High-Speed Imaging Receiver Design for 6G Optical Wireless Communications: A Rate-FOV Trade-Off

Mohammad Dehghani Soltani, Hossein Kazemi, Elham Sarbazi, Taisir E. H. El-Gorashi, Jaafar M. H. Elmirghani, Richard V. Penty, Ian H. White, Harald Haas and Majid Safari

Abstract

The design of a compact high-speed and wide field of view (FOV) receiver is challenging due to the presence of two well-known trade-offs. The first one is the area-bandwidth trade-off of photodetectors (PDs) and the second one is the gain-FOV trade-off due to the use of optics. The combined effects of these two trade-offs imply that the achievable data rate of an imaging optical receiver is limited by its FOV, i.e., a rate-FOV trade-off. In this paper, we propose an imaging receiver design in the form of an array of (PD) arrays. To control the area-bandwidth trade-off, small PDs are used in an array of arrays structure instead of a single large PD. Moreover, to achieve a reasonable receiver FOV, we use an array of focusing lenses that focus the light individually on each inner PD array. The proposed array of arrays structure provides an effective method to control both gain-FOV trade-off (via an array of lenses) and area-bandwidth trade-off (via arrays of small PDs). We first derive a tractable analytical model for the signal-to-noise ratio (SNR) of an array of PDs that is equipped with a focusing lens assuming maximum ratio combining (MRC). Then, we extend the model to the proposed array of arrays structure and the accuracy of the analytical model is verified based on several Optic Studio-based simulations. Next, we formulate an optimization problem to maximize the achievable data rate of the imaging receiver subject to a minimum required FOV. The optimization problem is solved for two commonly used modulation techniques, namely, on-off keying (OOK) and direct current (DC) biased optical orthogonal frequency division multiplexing (DCO-OFDM) with variable rate quadrature amplitude modulation (QAM). Our results show the limits of high speed wide-FOV imaging receivers that can support mobility. For example, it is demonstrated that a data rate of ~ 24 Gbps with a FOV of $15°$ is achievable using OOK with a total receiver size of 2 cm $\times 2$ cm.

I. INTRODUCTION

The global demand for high-speed data rate is increasing rapidly, where no saturation trends have yet been observed [2]. Three-dimensional (3D) holographic displays with the ability to

create virtual reality (VR) environments, 8K ultra-high-definition (UHD) video streaming and online video games are just few examples of applications that require high-speed data rate. It is forecasted there will be 5.7 billion connected mobile users by 2023 [3]. This yields an exponential growth in data traffic of wireless communications. The radio frequency (RF) may struggle to handle this high data traffic. In fact, RF spectrum is getting congested and wireless devices are seriously interfering with each other. As a result, the data throughput of the devices is affected severely, and the established connection may be poor.

Optical wireless communication (OWC), which permits the availability of a huge spectrum, is a propitious technology to alleviate the RF spectrum congestion by offering solutions such as (i) free space optical (FSO) communications [4], (ii) visible light communications (VLC) [5], (iii) underwater OWC [6], (iv) optical camera communications (OCC) [7] and (v) wireless networking with light, which is also referred to as LiFi [8]–[10]. Moreover, OWC can create smaller communication cells in the network, known as attocell [8] which is a vital key to unlock the path to exponential capacity growth for indoor scenarios [11]. OWC can offload heavy traffic loads from congested RF wireless networks, therefore making the RF spectrum to be available for emerging wireless applications such as the Internet of Things (IoT).

High-speed aggregate Terabit per second indoor OWC systems are being realized thanks to the large modulation bandwidth of laser diodes [12]–[16]. Hong *et al.* demonstrated that a ten-channel wavelength division multiplexing (WDM) intensity modulation/direct detection (IM/DD) system can achieve > 1 Tb/s capacity at a distance of 3.5 m with a lateral coverage up to 1.8 m [12]. A 1 Tbit/s bi-directional free-space connection has been presented in [13], which employs ten WDM channels with pulse amplitude modulation (PAM)-4. The coverage area of 2.54 m^2 is reported. Beam-steering laser-based optical multiuser systems, which are capable of supporting up to 128 beams carrying up to 112 Gbit/s per beam has been developed in [14].

One of the major challenges for the full adoption of OWC in 6G indoor wireless networks is to design high-speed optical receivers that can operate reliably in a mobile environment. Such receiver requires small detectors with large bandwidth and a large FOV[1] to support mobility. However, enabling a high data rate and a large FOV at the same time is challenging due to the following reasons. Firstly, there is a trade-off between photodetector (PD) bandwidth and its sensitive area. The utilization of light-focusing optics (lens or concentrator) can compensate for

---

[1]It is noted that throughout this paper, FOV is defined based on the full-cone angle.

the small area of a high-bandwidth PD and enhance the received signal-to-noise ratio (SNR). However, the use of optics gives rise to a second trade-off between gain and the FOV of the receiver in accordance with etendue law of conservation [17]. This indicates that the improved SNR is achieved in expense of a narrow FOV receiver.

The choice of angle diversity receiver (ADR), which consists of multiple narrow-FOV detectors facing different directions, is one way to achieve a larger aperture and wider FOV [18]. In [19], a wide-FOV receiver using fused fiber-optic tapers is proposed, which comprises hundreds of thousands of tapered optical fibers. An overall FOV of $30°$ and optical gain of 121.3 are reported. However, receiver designed based on these approaches are not as compact as typical imaging receivers. Two different receiver structures with wide FOV have been introduced for multiple-input multiple-output (MIMO) systems which enhance the condition of channel matrices [20], [21] and improve the diversity gain by employing aperture-based receivers [20] and different FOVs at the receiver [21]. It is shown to separate signal received from different directions with low multistream interference. Fluorescent optical concentrators are also introduced to enhance the receiver FOV, which are mainly applicable for visible light communications [22]–[24]. A fluorescent concentrator is shown to achieve a gain of 50 times higher than the conventional concentrators with the same FOV [22]. In [24], a threefold increment in data rate is reported by using a fluorescent antenna that can support FOV of $120°$. However, the maximum data rates reported using this approach are still limited since color conversion restricts the bandwidth.

An array of PDs along with proper optics is another promising solution which can offer an enhanced SNR and a wide FOV while ensuring a compact design, which is essential for portable mobile devices. Detector arrays can be designed using PIN or avalanche photodiodes (APD), which typically operate in thermal noise limited and shot noise limited regimes, respectively [25]. For mobile scenarios, positive-intrinsic-negative (PIN) photodetectors are more preferable due to low biasing voltage [26]. The output current of PIN photodetectors is typically so small that this necessitates the use of an amplifier. Among various types of amplifiers, transimpedance amplifiers (TIAs) are best suited to most optical wireless applications, since they support a large dynamic range and have a wide bandwidth without the need for an equalizer [18], [27]. High speed TIAs have been designed and fabricated in many studies [28]–[32]. For instance, TIAs with 66 GHz and 96 GHz bandwidth are demonstrated in [31] and [32], respectively. The other consideration when designing a detector array receiver is the choice of a combining technique, e.g., equal gain combining (EGC), selection combining (SC), switched combining (SWC) or the

maximal ratio combining (MRC). It has been mathematically proven that even though an array of PDs augments more noise, employing an efficient combining algorithm can help us achieve a superior probability of error performance compared to a single-detector receiver in practical channel conditions [33], [34].

Several experimental works in the literature have demonstrated the use of an array of PDs to achieve high data rates. In [35], a broadband receiver with a large aperture is introduced. The authors experimentally demonstrated a data rate of 1 Gbps at a FOV of $10°$. Umezawa *et al.* have reported an array of 8×8 pixels along with a 15 mm diameter-lens, which manifests a FOV of $6°$ in [36]. They have achieved data rate of 25 Gbps at a distance of 10 m. Signal detection enhancement for PD arrays has been discussed in [37]. Vilnrotter *et al.* have proposed an optimum array detection algorithm, which requires intensive computation and a simpler suboptimum structure that can achieve performance improvement up to 5 dB. All these studies emphasize the realization of high-speed mobile receiver by means of an array of PDs. However, to the best of our knowledge, there is no tractable analytical framework in the literature enabling imaging receiver designs that can optimally explore the trade-off between achievable data rate and FOV. In this study, we initially derive a general SNR model for a single array, where MRC technique is employed. Then, we extend the model for an array of arrays. Afterwards, we develop an optimization problem to design an imaging receiver with maximum achievable data rate supporting a required FOV. The contributions of this paper are summarized as follows:

- In-depth analysis of an imaging optical receiver by modeling beam spot size considering both focused and defocused designs for the imaging receiver.
- Development of a tractable framework for SNR of a static single array as well as the average SNR over different receiver tilt angles.
- Formulating an analytical optimization problem to achieve an optimum design for a receiver that can support required constraints such as a minimum FOV and maximum bit error rate (BER). The optimization problem has been evaluated for direct current (DC) biased optical orthogonal frequency division multiplexing (DCO-OFDM) with variable rate quadrature amplitude modulation (QAM) and on-off keying (OOK).
- Validating analytical models and derivations using realistic simulations conducted in Optic-Studio (Zemax) software.
- Presenting insightful results and detailed discussions about the impact of various trade-offs on receiver design, in the presence of non-idealities and practical aspects of the imaging
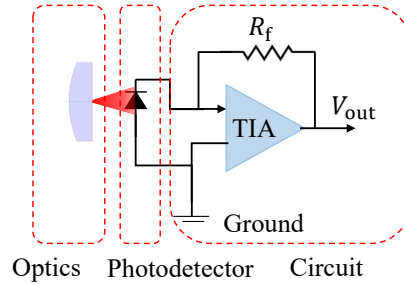
Fig. 1: A common structure of an optical wireless receiver.

receiver components.

The rest of this paper is organized as follows. In Section II, the area-bandwidth and gain-FOV trade-offs are discussed. In Section III, we present analytical framework of SNR for a single array as well as an array of arrays. In Section IV, the optimization problem is formulated to obtain the optimum design of a high-speed receiver. Simulation results are presented in Section V. In Section VI, summary and concluding remarks of this study are drawn and a number of possible directions are suggested for the future research.

II. DESIGN TRADE-OFFS FOR HIGH-SPEED OWC RECEIVERS

A common architecture of a receiver for OWC is shown in Fig. 1, which includes three main elements: a photodiode (PD), optics and a TIA. The proper selection of these elements plays a crucial role in addressing the design trade-offs as well as fulfilling the system requirements such as a desired data rate, FOV, and bit error ratio (BER). High bandwidth PDs are more favorable for high-speed applications, however, the higher the bandwidth, the smaller the sensitive area. This is recognized as the area-bandwidth trade-off and states that a high bandwidth PD may not be able to collect sufficient power, particularly when the beam spot radius at the receiver is much larger than the PD side length. Furthermore, choosing high bandwidth PDs in a power-limited regime is not a good practice as it adds more noise to the system, resulting in SNR degradation. The use of imaging optics in front of the PD can help to collect more power and improve the SNR. However, the FOV of the receiver will be limited due to the law of conservation of etendue [17], resulting in a gain-FOV trade-off. Next, we will discuss the area-bandwidth and gain-FOV trade-offs in more details.

A. Area-Bandwidth Trade-off

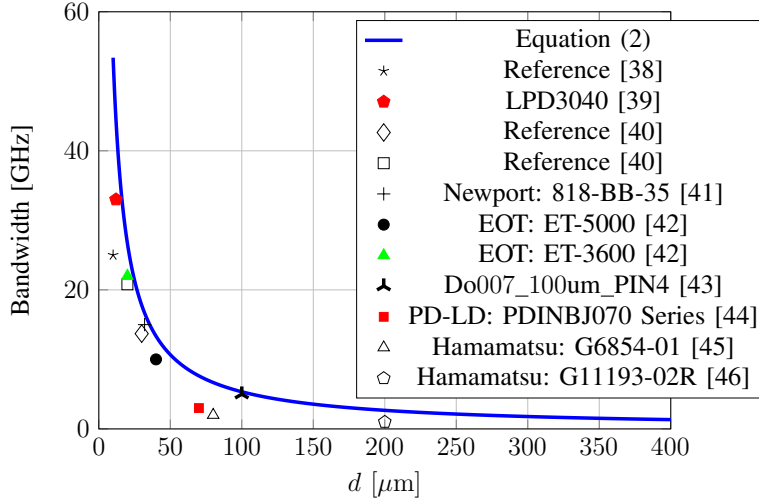The bandwidth of PIN photodetectors is expressed as [25]:

Fig. 2: Bandwidth versus the side length of a PIN photodetector, presenting the area-bandwidth trade-off. Several practical and commercial PIN PDs have been included.

$$B = \frac{1}{\sqrt{\left(2\pi R_{\mathrm{s}}\epsilon_0\epsilon_{\mathrm{r}}\dfrac{A}{\ell}\right)^2 + \left(\dfrac{\ell}{0.44v_{\mathrm{s}}}\right)^2}}, \tag{1}$$

where R_{s} is the junction series resistance, ϵ_0 is the permittivity in vacuum (8.85×10^{-12} F.m^{-1}) and ϵ_{r} is the relative permittivity of the semiconductor. The area and the length of the depletion region are denoted by A and ℓ, respectively. Also, v_{s} is the carrier saturation velocity which is limited by the hole saturation velocity. The junction series resistance, R_{s}, typically varies from 7 Ω to 9 Ω depending on the PD size [47]. If the PD is followed by a TIA with an input resistance of R_{L}, that is typically 50 Ω for commercial products, the bandwidth is affected. In this case, R_{s} in (1) should be replaced by the overall resistance $R_{\mathrm{s}} + R_{\mathrm{L}}$ [25].

The left and right terms under the radical sign in (1) represent the junction capacitance and transit time of a PIN detector, respectively. Clearly, as ℓ increases junction capacitance decreases, yielding a bandwidth increment, while the transit time increases, causing a bandwidth decrements. This trade-off results in an optimum length of depletion region which is denoted by ℓ_{opt} [25]. Assuming a square shape for the PD with a side length of d, after some manipulations of (1), the optimal bandwidth at $\ell = \ell_{\mathrm{opt}}$ can be rewritten as:

$$B = \frac{1}{C_{\mathrm{t}}d}, \qquad \text{where} \qquad C_{\mathrm{t}} = \sqrt{\frac{4\pi R_{\mathrm{s}}\epsilon_0\epsilon_{\mathrm{r}}}{0.44v_{\mathrm{s}}}}, \tag{2}$$

This equation is an upper bound for bandwidth and other depletion regions where $\ell \neq \ell_{\mathrm{opt}}$ result in a lower value for bandwidth.

Fig. 2 illustrates the bandwidth versus side length of a photodetector for $\ell = \ell_{\mathrm{opt}}$, which provides a theoretical upper bound on the performance of practical detectors. For comparison,
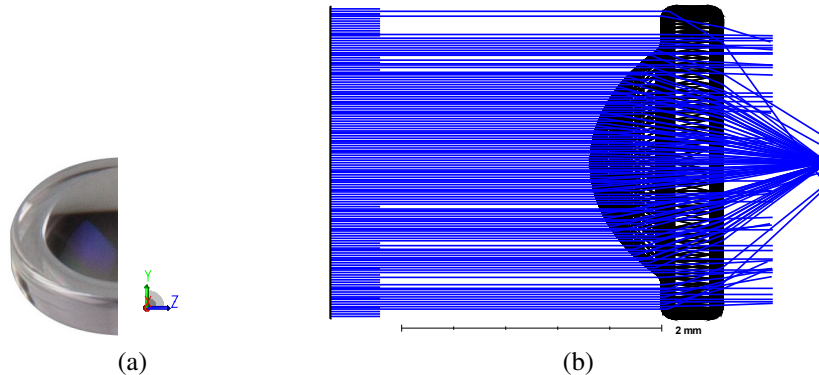
(a)

(b)

Fig. 3: Thorlabs 354140-B aspheric lens: (a) unmounted, (b) ray tracing simulations in OpticStudio [48].

TABLE I: Thorlabs 354140-B aspheric lens specifications [49].

Effective focal length	Outer diameter	Back focal length	Clear aperture	Glass	refractive index @ 850 nm
1.45 mm	2.4 mm	0.82 mm	1.6 mm	D-ZK3	1.5809

we have included several commercial PDs in Fig. 2, which show the tightness of the theoretical bound. Note that the area-bandwidth trade-off can be observed from these results, where as d (or equivalently A) increases, the bandwidth decreases. When the received optical power is sufficiently high, the selection of high bandwidth PDs are preferred to achieve high data rates.

B. Gain-FOV Trade-off

The use of optics boosts the collected optical power at the expense of a reduced receiver FOV, i.e., the gain-FOV trade-off. In this paper, we focus on using an imaging lens and the study of compound parabolic concentrator (CPC) is kept for future investigations. Without loss of generality, in this study, we employ an aspheric lens. We calculate the beam spot radius after the lens and the FOV as a function of distance between the lens and the PD. These two functions are essential in the SNR analysis and optimal design of receiver. Compared to other types of lenses, aspheric ones are known to produce a precise and small beam spots due to spherical aberration correction. Also, the generated beam spot after an aspheric lens is almost uniform. As an example, we consider a Thorlabs aspheric lens with the specifications given in Table I and the geometry shown in Fig. 3. We note that the following theoretical analyses can be extended to other imaging lenses.

Let L denote the distance between the aspheric lens and the observing plane and $W_2(L)$ denote the beam spot radius after the lens. The fraction of the total beam power contained by $W_2(L)$ is denoted by η in this study. Fig. 4a illustrates $W_2(L)$ at different values of L for $\eta = 0.5$
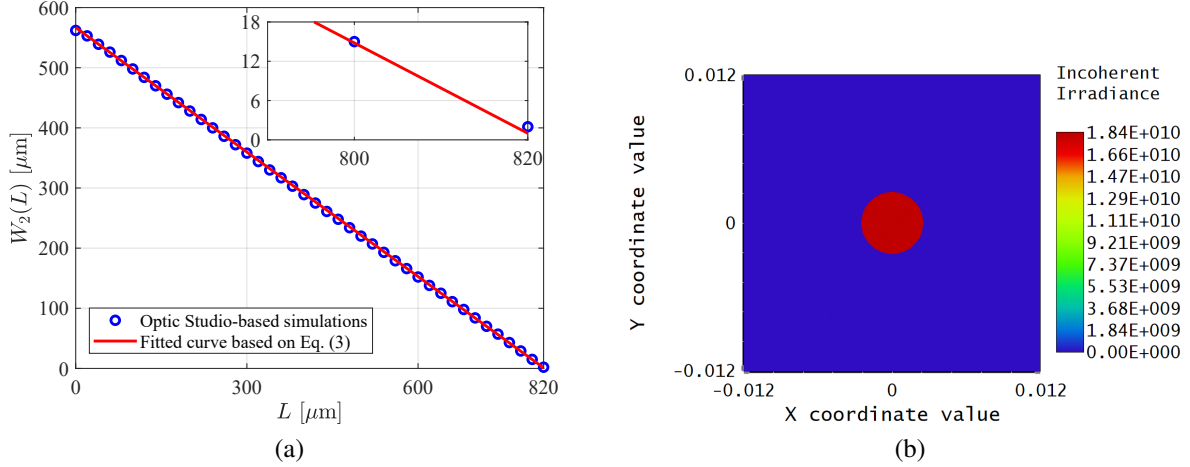
Fig. 4: (a) Beam spot radius versus distance from the lens obtained from OpticStudio software and the fitted curve with $b_1 = 0.69$ and $b_0 = 1$ μm, (b) beam spot at $L = 820$ μm in OpticStudio (dimensions are in mm).

the Thorlabs 354140-B aspheric lens. The values of $W_2(L)$ are obtained using the commercial optical design software, OpticStudio [48]. According to Fig. 4a, the linear behavior of the beam spot radius versus L can be well approximated by:

$$W_2(L) = b_1(f_b - L) + b_0, \tag{3}$$

where f_b is the back focal length of the aspheric lens. The two constants b_0 and b_1 can be obtained from the clear aperture of the lens denoted by CA and the spot radius in the diffraction limit. Diffraction limit determines the maximum resolution that can be achieved by an optical component. It is defined as $r_{DL} = 1.22\lambda f_e/CA$, where λ is the wavelength of the light, and f_e is the effective focal length of the lens [50]. Assuming that the incident beam spot is larger than the lens clear aperture, $W_2(L) = 0.5CA$ at $L = 0$. Also, as shown in Fig. 4b, at $L = 820$ μm, $W_2(L)$ is equal to the diffraction limit. Therefore, b_0 and b_1 are obtained as:

$$b_0 = r_{DL}\kappa, \tag{4a}$$

$$b_1 = \frac{\kappa}{2f_b}\left(CA - 2r_{DL}\right), \tag{4b}$$

where f_e and CA are the effective focal length and the clear aperture of the lens, respectively, which are provided in the datasheet [49]. In (4), κ is a constant parameter, which is $\kappa = \sqrt{\eta}$.

The thickness of the considered aspheric lens is 1 mm, which is comparable to its radius of curvature that is 0.84 mm [49]. Therefore, the lens is not a thin lens[2]. We therefore evaluate the relation between FOV and L using the OpticStudio simulator. We accentuate that the traditional tangent equation that describes the relation between the FOV and the effective focal length of

---

[2]A thin lens is a lens with a thickness that is negligible compared to the radii of curvature of the lens surfaces [51].

the lens [52] cannot be directly applied for all $0 \leq L \leq f_\mathrm{b}$. There are several important remarks to highlight before introducing the approximation of the FOV. Firstly, L and the back focal point, f_b, are measured from the back surface of the lens, while the effective focal length, f_e, is measured from the principal plane of the lens. Secondly, the traditional expression of FOV is applicable for L that ensures the condition of $W_2(L) \leq d/2$, i.e., the beam spot is inscribed inside the PD. Thirdly, the FOV is defined based on the half power metric. We can now present the approximation relation of FOV and L which is valid for $W_2(L) \leq d$ as:

$$\mathrm{FOV} = 2\tan^{-1}\left(\frac{d}{2(L + f_\mathrm{e} - f_\mathrm{b})}\right), \qquad \frac{b_0 - b_1 f_\mathrm{b} - d/2}{b_1} \leq L \leq f_\mathrm{b}, \qquad (5)$$

where the lower bound of L is obtained by solving $2W_2(L) = d$ and using (3).

The gain of a lens is defined as the ratio between the input and output aperture of the lens, i.e.,:

$$G = \frac{A_\mathrm{in}}{A_\mathrm{out}} = \frac{(r_\mathrm{lns})^2}{(W_2(L))^2}, \qquad (6)$$

where r_lns is the outer radius of the lens and $W_2(L)$ is the beam spot radius at distance L from lens which is given in (3). Therefore,

$$G = \frac{(r_\mathrm{lns})^2}{(b_1(f_\mathrm{b} - L) + b_0)^2}. \qquad (7)$$

From (5),we have $L = \frac{d}{2\tan(0.5\mathrm{FOV})} - (f_\mathrm{e} - f_\mathrm{b})$. Substituting this for L in (7), we have:

$$G = \frac{(r_\mathrm{lns})^2}{\left(b_1\left(2f_\mathrm{b} - \dfrac{d}{2\tan(0.5\mathrm{FOV})} - f_\mathrm{e}\right) + b_0\right)^2}. \qquad (8)$$

It can be inferred from the above equation that by increasing the FOV, G will reduce noting that the coefficients b_0 and b_1 are positive.

Fig. 5a-5c represent the normalized collected power at the PD, $\bar{P}_\mathrm{r}$, versus different tilt angles of transmitted beam about the X axis. These results are obtained in OpticStudio and the collected power is normalized to the value at zero tilt angle. Three separate locations are selected to exhibit the effect of tilt angle on the collected power. It can be observed that at $L = 400~\mu\mathrm{m}$ for the tilt angles between $-15.5°$ to $15.5°$ about the X axis, the normalized power is greater than 0.5. The range would be $[-10.5°, 10.5°]$ and $[-8°, 8°]$ at $L = 600~\mu\mathrm{m}$ and $L = 820~\mu\mathrm{m}$, respectively. One typical definition of the FOV is based on the half value of the collected power. Therefore, the FOV at $L = 400~\mu\mathrm{m}$, $L = 600~\mu\mathrm{m}$ and $L = 820~\mu\mathrm{m}$ are $33°$, $21°$ and $16°$, respectively. Fig. 5d illustrates the results of L versus FOV acquired in OpticStudio. A square PD with side
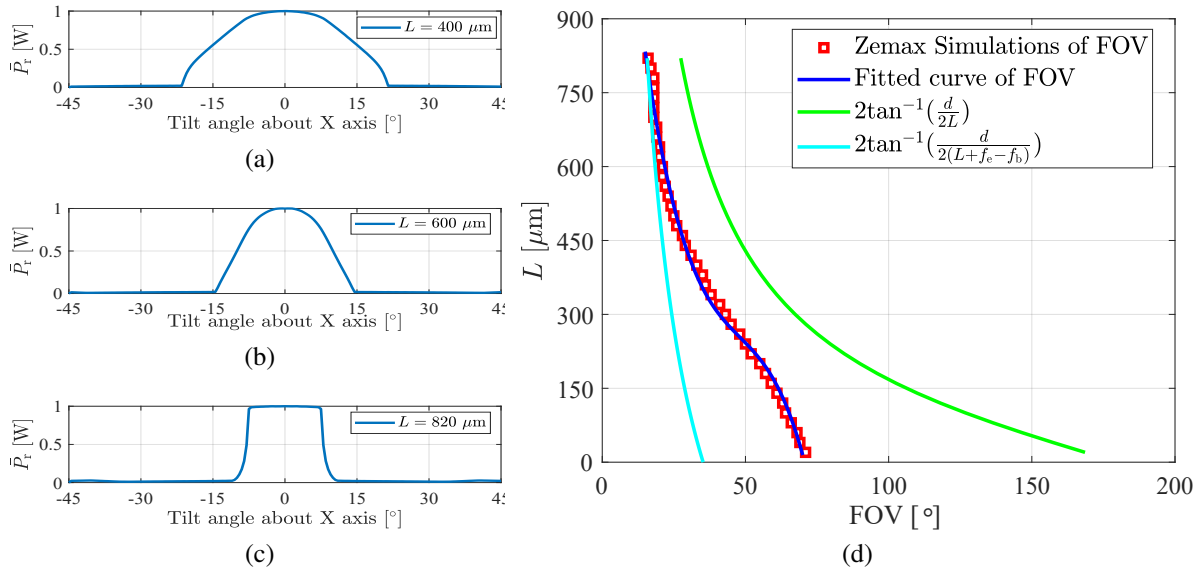
Fig. 5: Normalized received optical power versus transmitted beam tilt angle at (a) $L = 400$ μm, (b) $L = 600$ μm and (c) $L = 820$ μm. (d) L versus FOV obtained from OpticStudio software, the fitted curve and the conventional analytical model for FOV.

length of 400 μm is considered in these simulation results. The fitted curve to these results is:

$$L = a_3\text{FOV}^3 + a_2\text{FOV}^2 + a_1\text{FOV} + a_0, \tag{9}$$

where $(a_3, a_2, a_1, a_0) = (-0.08506, 6.142, -159.5, 1720)$ with a normalized root mean square error (NRMSE) of less than 10^{-4}. The values for (a_3, a_2, a_1, a_0) are obtained using the curve fitting toolbox of Matlab software. We have also plotted the approximation relation of FOV and L, which provides a good estimate for the range 520 μm $\leq$ L ≤ 820 μm. For comparison, the curve of $2\tan^{-1}(d/2L)$ has been included, where we can see there is a noticeable gap between this curve and the OpticStudio simulations without applying the impact of $f_\text{e} - f_\text{b}$.

C. Array of Arrays Receiver Structure

In an imaging optical receiver, the combined effect of the area-bandwidth and gain-FOV trade-offs introduces a new trade-off between the achievable data rate and FOV of the receiver, namely the rate-FOV trade-off. This is because for achieving higher data rate, more bandwidth (i.e., smaller PD) and higher collected power (i.e., larger collecting lens), which both imposing limits on the receiver FOV. In this paper, we propose an array of arrays structure for the imaging receiver that allows us to effectively control the area-bandwidth and gain-FOV trade-offs in order to achieve the desired system requirement, that is constrained by the rate-FOV trade-off.

Fig. 6a illustrates the the proposed array of arrays structure, in which $\mathcal{N}_\text{a}$ arrays are assumed to be arranged on a square lattice. It can be thus expressed as:
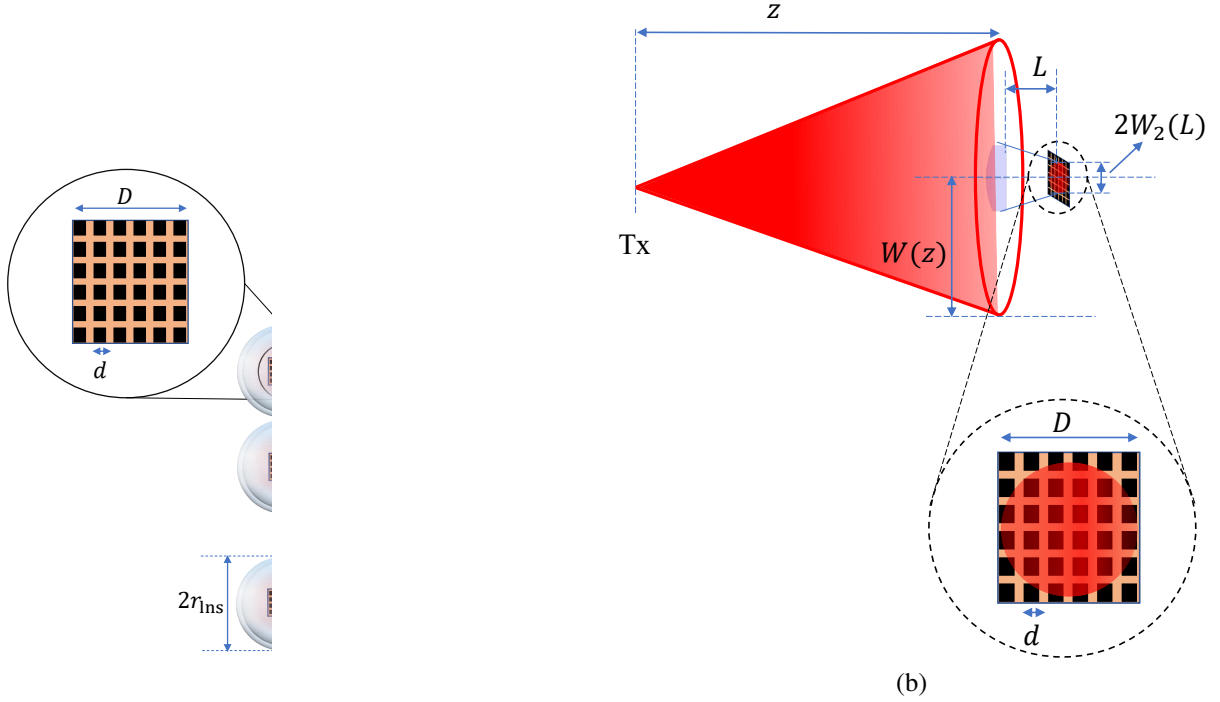
Fig. 6: (a) The proposed $\sqrt{\mathcal{N}_a} \times \sqrt{\mathcal{N}_a}$ array of arrays structure for imaging receiver, (b) geometry of beam spots and one array of PDs.

$$\mathcal{N}_a = \left(\frac{D_a}{2r_{\text{lns}}}\right)^2, \tag{10}$$

where D_a is the side length of the array of arrays receiver. In this structure, to produce a high received optical power, the combined output of the array of $\mathcal{N}_a$ imaging detectors are considered where each imaging detector includes an N_{PD} photodetector array equipped with a collecting lens placed at a distance of L from it (see Fig. 6b). Note that each array of PDs are assumed to be integrated into a single chip. Let the side length of each PD and the array be denoted by d and D, respectively. The fill factor (FF) of an array of N_{PD} PDs, which are arranged in a square lattice, can be described as:

$$\text{FF} = \frac{N_{\text{PD}}d^2}{D^2}. \tag{11}$$

Assuming that the overall size of the receiver is fixed, the size of the outer array (i.e., $\mathcal{N}_a$) controls the gain-FOV trade-off while the size of the inner arrays (i.e., N_{PD}) controls the bandwidth-area trade-off. Therefore the sizes of inner and outer arrays can be adjusted to achieve desired receiver performance in terms of data rate, FOV, and BER. Fixing the size of arrays, the key remaining control parameters are the side length of each PD, d, and the distance between the lens and PD array, L. Note that defocusing (i.e., reducing L below the focal length) can further increase the FOV of the receiver (see Fig. 6b). In the following sections, we will initially present the SNR
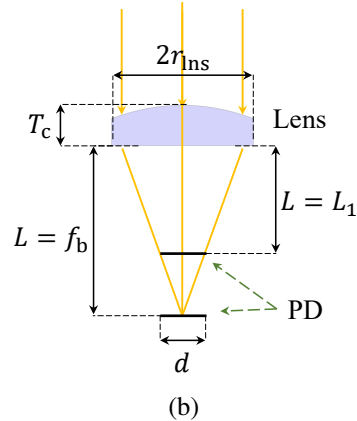
Fig. 7: (a) Geometry of CPC, (b) geometry of the aspheric lens and a PD.

analysis of an array of arrays and then, the problem formulation for an optimized design will be introduced.

D. Comparison Between Imaging and Non-imaging Receivers

Non-imaging receivers which consist of optics that do not produce an image of the source are the other well-known type of receivers in optical wireless communication. A compound parabolic concentrator (CPC) is a popular example of non-imaging optics. The geometry of a CPC is shown in Fig. 7a. The FOV of CPCs is defined based an acceptance angle, θ_a as:

$$\text{FOV}_{\text{CPC}} = 2\theta_a = 2\sin^{-1}\left(n\frac{D_{\text{out}}}{D_{\text{in}}}\right),\tag{12}$$

where D_{in} and D_{out} are the input and output aperture diameters of the CPC, respectively, and n is the refractive index of the CPC. The gain and height of a CPC are given below respectively [18], [53]:

$$\text{G} = \frac{n^2}{\sin^2(\theta_a)},\tag{13}$$

$$H = \frac{D_{\text{in}} + D_{\text{out}}}{2\tan(\theta_a)}.\tag{14}$$

We now compare the considered aspheric lens with parameters given in Table I with a CPC with an input diameter similar to the outer diameter of the lens, i.e., $D_{\text{in}} = 2.4$ mm. For a fair comparison, the refractive index of CPC is set to be the same as the aspheric lens, $n = 1.58$. As an example, let us consider a photodetector with a side length of $d = 400$ μm, in order to ensure the PD absorbs all collected power by the CPC on top of the PD, the constraint $D_{\text{out}} \leq d$ should be met. Using (12), the FOV of the CPC is $30.53°$ and based on (14), $H = 5.13$ mm. The aspheric lens Thorlabs 354140-B offers FOV of $24°$ at $L = 530$ μm based on Zemax simulations

TABLE II: Comparison between a CPC and a Lens.

	Non-imaging receivers (with CPC)	Imaging receivers (with lens)
Definition	cannot produce an image of the source after optics	produce an image of the source after optics
Advantage	Higher FOV Relaxed alignment	Able to focus the collected power on one PD Availability of varieties of lenses
Disadvantage	Higher length Difficult to manufacture [54]	Adjustment of the array at the focal point (alignment)
FOV	$2\theta_{\mathrm{a}}$	$2\tan^{-1}\left(\dfrac{d}{2f_{\mathrm{e}}}\right)$
Maximum height	$H = \dfrac{D_{\mathrm{in}} + D_{\mathrm{out}}}{2\tan(\theta_{\mathrm{a}})}$	$T_{\mathrm{c}} + f_{\mathrm{b}}$ T_{c}: thickness of the lens
Maximum gain	$\dfrac{n^2}{\sin^2(\theta_{\mathrm{a}})}$	$\dfrac{(r_{\mathrm{lns}})^2}{(1.22\lambda f_{\mathrm{e}}/\mathrm{CA})^2}$

(at $L = L_1 = 530$ μm, we have $W_2(L) = 200$ μm). The height of this receiver would be the sum of the thickness of the lens and $L = 530$ μm, (i.e., $T_{\mathrm{c}} + L_1$), which is 1.53 mm. The gain and SNR of these two imaging and non-imaging receivers are similar. As another example, for a PD with side length of $d = 60$ μm, the CPC offers FOV of a $4.54°$ with a height of 31.11 mm, while the same ashpheric lens, Thorlabs 354140-B, suggests a FOV of $2.44°$ with total height of 1.78 mm. In contrast to CPCs, we can place PDs at different distances from lens, which allows us to achieve various FOVs as shown in Fig. 7b. The gain and SNR of these two imaging and non-imaging receivers are similar since the input and output of their optics are set to be the same. Therefore, the offered achievable data rates of both imaging and non-imaging designs are the same. However, the imaging receivers suggest a more compact design, still with a reasonable FOV compared to the non-imaging counterparts. Furthermore, aspheric lenses are available commercially from small diameters (few millimeters) to large diameters (tens of centimeters), while the range of CPC is limited due to less commercial demand [54]. Therefore, in this research paper, we focus on the imaging receiver and design of an optimized non-imaging receiver is the focus of our future study [55]. Table II summarize the comparison between non-imaging and imaging optics.

III. SNR ANALYSIS OF THE ARRAY OF ARRAYS RECEIVER

We assume that a lens of radius r_{lns} is placed in front of the array, as shown in Fig. 6b. It is also assumed that each PD in the array is individually connected to a high bandwidth TIA,

since the output current of PIN photodetectors are typically small. Under this assumption, the receiver bandwidth is limited by the PD's bandwidth.

Three types of noise can affect the performance of this receiver; thermal, shot and relative intensity noise (RIN) noise [15], [16]. The dominant noise source is the TIA thermal noise whose variance is given by [18], [25]:

$$\sigma_{\mathrm{n}}^2 = \frac{4k_{\mathrm{b}}TF_{\mathrm{n}}B}{R_{\mathrm{f}}}, \tag{15}$$

where k_{b} is the Boltzmann constant, R_{f} is the feedback resistor of the TIA, T is temperature in Kelvin, F_{n} is the noise figure of the TIA and B is the bandwidth of the PIN photodetector.

Different combining methods such as MRC, equal gain combining (EGC) and selection combining (SC) can be used to combine the output of PDs. Typically, MRC outperforms the other two techniques while requiring a more complex hardware circuit. In this paper, we provide the analyses for MRC, however, they can be extended to EGC and SC in a similar way. In the following, we start by deriving the SNR of the MRC technique for a single array shown in Fig. 6a. Next, we will extend our analysis to an array of $\sqrt{\mathcal{N}_{\mathrm{a}}} \times \sqrt{\mathcal{N}_{\mathrm{a}}}$ PD arrays as illustrated in Fig. 6b. We will then suggest a threshold-based selection EGC (TS-EGC) with lower complexity than MRC .

The SNR of MRC technique for a single array can be obtained as [56]:

$$\gamma_{\mathrm{MRC}} = \sum_{i=1}^{N_{\mathrm{PD}}} \gamma_i, \tag{16}$$

where γ_i is the SNR of the ith PD, which is:

$$\gamma_i = \frac{(R_{\mathrm{res}}P_{\mathrm{r},i})^2}{\sigma_{\mathrm{n}}^2}, \tag{17}$$

where R_{res} is the PD responsivity, σ_{n}^2 is the variance of noise given in (15), and $P_{\mathrm{r},i}$ denotes the received optical power of the ith PD. $P_{\mathrm{r},i}$ depends on the beam spot radius after the lens, $W_2(L)$, which is expressed by (3) and is shown in Fig. 6b.

The radius of beam spot at the receiver plane is denoted by $W(z)$, where it is assumed that $W(z) \gg r_{\mathrm{lns}}$. Thus, we can assume almost a uniform beam intensity over the whole area of the lens. Furthermore, ray-tracing simulations conducted in OpticStudio [48] confirm that the beam after the lens has almost a uniform intensity profile. Accordingly, $P_{\mathrm{r},i}$ can be readily calculated as:

$$P_{\mathrm{r},i} = \iint\limits_{\mathcal{A}_i} \frac{\xi P_{\mathrm{r,lns}}}{\pi W_2^2(L)} \, dx \, dy = \xi P_{\mathrm{r,lns}} \frac{\mathcal{A}_i}{\pi W_2^2(L)}, \tag{18}$$
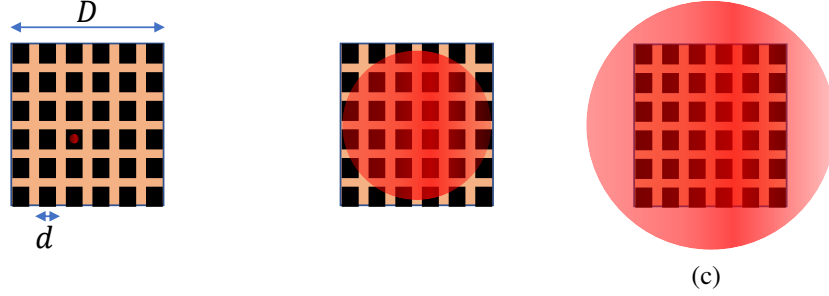
Fig. 8: Illustration of different conditions of beam spot radius for an array of PDs.

where $\mathcal{A}_i$ denotes the overlapping area of beam after the lens and the ith PD. Also, $\xi = \xi_{\mathrm{r}}\xi_{\mathrm{p}}\xi_{\mathrm{a}}$; with ξ_{r} representing the transmission coefficient of the lens; $\xi_{\mathrm{p}} = 0.5$ due to definition of spot radius being the minimum radius that includes 50% of total power and $\xi_{\mathrm{a}} = \mathrm{CA}^2/(2r_{\mathrm{lns}})^2$, where CA is the clear aperture. In (18), $P_{\mathrm{r,lns}}$ is the power collected by the lens with the radius of r_{lns}. Based on the relation between $W_2(L)$, D and d, there are separate cases for $P_{\mathrm{r},i}$. For example, as shown in Fig. 8a, a small beam spot radius can result in detecting the whole collected power by lens. When considering these three possible conditions, the received power by each detector can be expressed as:

$$
P_{\mathrm{r},i} = \begin{cases} \xi P_{\mathrm{r,lns}}\rho_i, & W_2(L) \leq \dfrac{1}{\sqrt{\pi}}d, \\[2mm] \xi P_{\mathrm{r,lns}}\dfrac{\mathcal{A}_i}{\pi W_2^2(L)}, & \dfrac{1}{\sqrt{\pi}}d < W_2(L) \leq \dfrac{1}{\sqrt{\pi}}D, \\[2mm] \xi P_{\mathrm{r,lns}}\dfrac{d^2}{\pi W_2^2(L)}, & W_2(L) > \dfrac{1}{\sqrt{\pi}}D. \end{cases}
\tag{19}
$$

where $\rho_i = 1$ if the beam spot after lens hits a detector and $\rho_i = 0$ if it does not. Note that, for simplification, in the case of $W_2(L) \leq \frac{1}{\sqrt{\pi}}d$, which is equivalent of a small beam spot at the detector plane (see Fig. 8a), we approximate the received power by assuming that the whole beam is either detected by a single PD or not detected at all. Moreover, in the case of $W_2(L) > \frac{1}{\sqrt{\pi}}D$, where the beam spot covers the whole array (see Fig. 8c), each detector would be fully illuminated thereby $\mathcal{A}_i = d^2$. Substituting (19) into (17) and then into (16), the SNR of MRC technique for a single array is obtained as:

$$
\gamma_{\mathrm{MRC}} = \dfrac{1}{\dfrac{4k_{\mathrm{b}}TF_{\mathrm{n}}B}{R_{\mathrm{f}}}} \times \begin{cases} \rho\left(R_{\mathrm{res}}\xi P_{\mathrm{r,lns}}\right)^2, & W_2(L) \leq \dfrac{1}{\sqrt{\pi}}d, \\[3mm] \left(\dfrac{R_{\mathrm{res}}\xi P_{\mathrm{r,lns}}}{\pi W_2^2(L)}\right)^2 \displaystyle\sum_{i=1}^{N_{\mathrm{PD}}} \mathcal{A}_i^2, & \dfrac{1}{\sqrt{\pi}}d < W_2(L) \leq \dfrac{1}{\sqrt{\pi}}D, \\[3mm] N_{\mathrm{PD}}\left(R_{\mathrm{res}}\xi P_{\mathrm{r,lns}}\dfrac{d^2}{\pi W_2^2(L)}\right)^2, & W_2(L) > \dfrac{1}{\sqrt{\pi}}D. \end{cases}
\tag{20}
$$

where $\rho = 1$ if the beam spot after lens hits one of the detectors in the array and $\rho = 0$ if it does not. Let us now calculate the mean SNR at the output of the proposed array of arrays receiver illustrated in Fig. 6a by averaging over different received angle of arrivals of the beam within the FOV of the receiver. The change of the beam angle of arrival will be equivalent to the shift of beam spot on the PD array plane. This means that in the case of large beam spot, $W_2(L) > \frac{1}{\sqrt{\pi}}D$, the detected power does not vary significantly by changing the angle of arrival of the beam and therefore the mean SNR would be approximately equal to the SNR given in (20). Furthermore, in the case of intermediate beam size (i.e., $\frac{1}{\sqrt{\pi}}d < W_2(L) \leq \frac{1}{\sqrt{\pi}}D$), we can approximate the mean value of $\sum\limits_{i=1}^{N_{\mathrm{PD}}} \mathcal{A}_i^2$ averaged over random shifts of beam spot as

$$E\left[\sum_{i=1}^{N_{\mathrm{PD}}} \mathcal{A}_i^2\right] \approx N_{\mathrm{act}}A^2 = \pi W_2^2(L)\mathrm{FF}d^2, \tag{21}$$

where $N_{\mathrm{act}} \approx \pi W_2^2(L)\mathrm{FF}/d^2$ is the average number of fully illuminated PDs and $A = d^2$ is the area of a single PD. Finally, in the case of a small beam spot (i.e., $W_2(L) \leq \frac{1}{\sqrt{\pi}}d$), the mean SNR can be estimated based on the probability of beam hitting a detector considering its random change of angle of arrival within FOV, which is given by $E[\rho] = \mathrm{FF}$. Therefore, the average SNR of MRC can be approximated as follows:

$$\overline{\gamma}_{\mathrm{MRC}} = \frac{\sqrt{\mathcal{N}_{\mathrm{a}}}}{\frac{4k_{\mathrm{b}}TF_{\mathrm{n}}B}{R_{\mathrm{f}}}} \times \begin{cases} (R_{\mathrm{res}}\xi P_{\mathrm{r,lns}})^2\mathrm{FF}, & W_2(L) \leq \frac{1}{\sqrt{\pi}}d, \\[2mm] (R_{\mathrm{res}}\xi P_{\mathrm{r,lns}})^2\dfrac{d^2}{\pi W_2^2(L)}\mathrm{FF}, & \frac{1}{\sqrt{\pi}}d < W_2(L) \leq \frac{1}{\sqrt{\pi}}D, \\[2mm] N_{\mathrm{PD}}\left(R_{\mathrm{res}}\xi P_{\mathrm{r,lns}}\dfrac{d^2}{\pi W_2^2(L)}\right)^2, & W_2(L) > \frac{1}{\sqrt{\pi}}D. \end{cases} \tag{22}$$

Note that the accuracy of the approximated average SNR above will be verified in section V. The EGC is known to have low complexity as it simply adds up the received power with equal weights. To reduce the complexity of MRC, we propose a modified version of EGC which we call threshold-based selection EGC (TS-EGC) that simply adds the output of those PDs with the output current above a certain threshold. It will be shown in section V that the MRC and TS-EGC perform similarly. Therefore, unless otherwise stated, we focus on the MRC technique to derive closed-form analytical solutions for the optimum designs.

IV. OPTIMUM GEOMETRIC DESIGN OF HIGH-SPEED RECEIVER

In this section, assuming a fixed size for inner arrays, we aim to optimize the side length of each PDs in the array, d, as well as the distance between the lens and the array, L, to achieve

the maximum data rate while satisfying a desired receiver FOV. In order to develop a compact receiver, L is assumed to be limited to the range $0 \leq L \leq f_{\mathrm{b}}$. That is, the lens is not placed at a distance more than its focal length from the PD array. This allows for both focused ($L = f_{\mathrm{b}}$) and defocused ($L < f_{\mathrm{b}}$) designs while the latter can relax the FOV constraint to some degree. It will be shown that the optimum value of L can be specified according to the desired FOV. In addition, the optimum value of d is selected in such a way that it achieves the maximum data rate while fulfilling the required BER (or SNR). We note that although small PDs have a higher bandwidth, they add more noise to the system thereby degrading the SNR. On the other hand, large area PDs decrease the system bandwidth and consequently the achievable data rate. Such a behavior in a power-limited regime yields an optimum d that maximizes the data rate. The optimization problem can be formulated as:

$$\max_{L,d} \quad R \tag{23a}$$

$$\text{s.t.} \quad \mathrm{FOV}(L) \geq \mathrm{FOV}_{\mathrm{req}}, \tag{23b}$$

$$\overline{\gamma}_{\mathrm{MRC}}(L, d) \geq \gamma_{\mathrm{req}}, \tag{23c}$$

$$d_{\min} \leq d \leq d_{\max} = D\sqrt{\frac{\mathrm{FF}}{N_{\mathrm{PD}}}}. \tag{23d}$$

The first constraint guarantees the FOV requirement and leads to an upper bound on L as $L \leq L_{\max}$, where $L_{\max}$ can be obtained by substituting $\mathrm{FOV}_{\mathrm{req}}$ in (9) as:

$$L_{\max} = a_3 \mathrm{FOV}_{\mathrm{req}}^3 + a_2 \mathrm{FOV}_{\mathrm{req}}^2 + a_1 \mathrm{FOV}_{\mathrm{req}} + a_0. \tag{24}$$

The second constraint enforces limitations on both the size of PDs and the distance between the lens and the array. In fact, SNR is directly related to d and L, where small values of d and L result in lower SNRs. By substituting (2) and (11) into (22), we can express this relationship as:

$$\overline{\gamma}_{\mathrm{MRC}} = \frac{1}{A_x} \times \begin{cases} d^3, & W_2(L) \leq \frac{1}{\sqrt{\pi}} d, \\ \dfrac{d^5}{\pi W_2^2(L)}, & \frac{1}{\sqrt{\pi}} d < W_2(L) \leq \frac{1}{\sqrt{\pi}} D, \\ D^2 \dfrac{d^5}{(\pi W_2^2(L))^2}, & W_2(L) > \frac{1}{\sqrt{\pi}} D, \end{cases} \tag{25}$$

where

$$A_x = \frac{4 k_{\mathrm{b}} T F_{\mathrm{n}} D^2}{N_{\mathrm{PD}} \sqrt{\mathcal{N}_{\mathrm{a}}} C_{\mathrm{t}} R_{\mathrm{f}} (R_{\mathrm{res}} \xi P_{\mathrm{r,lns}})^2}. \tag{26}$$

In constraint (23c), γ_{req} is the required SNR to ensure that BER is less than a target BER, i.e., $\mathrm{BER}_{\mathrm{req}}$. The threshold for SNR can be represented based on the BER requirement as [57]:

$$\gamma_{\mathrm{req}} = \left(Q^{-1}(\mathrm{BER}_{\mathrm{req}}) \right)^2, \tag{27}$$

where $Q^{-1}(\cdot)$ is the inverse of Q-function. The size of each PD on the array is limited to $d_{\min}$ and $D\sqrt{\frac{\mathrm{FF}}{N_{\mathrm{PD}}}}$. The right side of the third constraint is obtained based on (11) and ensures the fill factor of the array is limited to FF. To guarantee that the designed inner arrays follow a square lattice configuration, the number of PDs on each array are selected from the set of square numbers. The transmit power in this optimization problem is set to the maximum permissible value according to the eye safety regulations, i.e., $P_{\mathrm{t}} = P_{\mathrm{t,max}}$. The details of the eye safety considerations for obtaining $P_{\mathrm{t,max}}$ can be found in [58]. The optimization problem in (23) along with the piecewise SNR function in (25) can be broken down into three separate optimization problems, where the global solution will be the optimal solution among the three possible solutions. These optimization problems are expressed below.

Optimization problem 1:

$$\max_{d,L} \quad R \tag{28a}$$

$$\text{s.t.} \quad \mathrm{FOV}(L) \geq \mathrm{FOV}_{\mathrm{req}}, \tag{28b}$$

$$\frac{d^3}{A_x} \geq \gamma_{\mathrm{req}}, \tag{28c}$$

$$d_{\min} \leq d \leq D\sqrt{\frac{\mathrm{FF}}{N_{\mathrm{PD}}}}, \tag{28d}$$

$$d \geq \sqrt{\pi} W_2(L). \tag{28e}$$

Optimization problem 2:

$$\max_{d,L} \quad R \tag{29a}$$

$$\text{s.t.} \quad \mathrm{FOV}(L) \geq \mathrm{FOV}_{\mathrm{req}}, \tag{29b}$$

$$\frac{d^5}{A_x \pi W_2^2(L)} \geq \gamma_{\mathrm{req}}, \tag{29c}$$

$$d_{\min} \leq d \leq D\sqrt{\frac{\mathrm{FF}}{N_{\mathrm{PD}}}}, \tag{29d}$$

$$W_2(L) > \frac{d}{\sqrt{\pi}}, \tag{29e}$$

$$W_2(L) \leq \frac{1}{\sqrt{\pi}} D. \tag{29f}$$

Optimization problem 3:

$$\max_{d,L} \quad R \tag{30a}$$

$$\text{s.t.} \quad \mathrm{FOV}(L) \geq \mathrm{FOV}_{\mathrm{req}}, \tag{30b}$$

$$\frac{d^5}{A_x \left(\pi W_2^2(L)\right)^2} D^2 \geq \gamma_{\text{req}}, \tag{30c}$$

$$d_{\min} \leq d \leq D\sqrt{\frac{\text{FF}}{N_{\text{PD}}}}, \tag{30d}$$

$$W_2(L) > \frac{1}{\sqrt{\pi}} D. \tag{30e}$$

In what follows, we solve these optimization problems for two well-known and practical modulation schemes; DCO-OFDM with adaptive QAM and OOK.

A. DCO-OFDM

To ensure a high spectral efficiency with intensity modulation and direct detection, we here implement the DC-biased optical OFDM with adaptive QAM. By properly choosing the variance of the OFDM signal and the DC bias, a tight upper bound for the achievable data rate is given by [15], [16]:

$$R = \nu B \log_2 \left(1 + \frac{\overline{\gamma}_{\text{MRC}}}{\Gamma}\right), \tag{31}$$

where $\nu = \frac{N_{\text{sc}}-2}{N_{\text{sc}}}$ with N_{sc} denoting the number of subcarriers. In this equation, B is the single-sided bandwidth of the receiver. In (31), Γ represents the SNR gap due to the required BER, which is given by:

$$\Gamma = \frac{-\ln(5\text{BER}_{\text{req}})}{1.5}. \tag{32}$$

The optimization problem defined in (23) can be applied here to find the optimum side length of PDs and the distance between the lens and the inner array to maximize the data rate. Here, R is a differentiable function with respect to (w.r.t) d and L, showing different behaviors in different optimization problems discussed above. We now solve the optimization problems given in (28), (29) and (30) for DCO-OFDM.

Optimization problem 1: In this case, the objective function of (28) defined in (31) can be expressed as:

$$R = \frac{\nu}{C_t d} \log_2 \left(1 + \frac{d^3}{\Gamma A_x}\right). \tag{33}$$

The function in (33) is only a function of d and can be shown to have a unique maximum at:

$$d_* = (15.8\Gamma A_x)^{\frac{1}{3}}. \tag{34}$$

The proof is given in Appendix A. The objective function also has a minimum at $d = 0$ which is outside the feasible set. We should identify whether the possible solution given by (34) is within the feasible region of the problem 1. The second constraint of (28) implies:

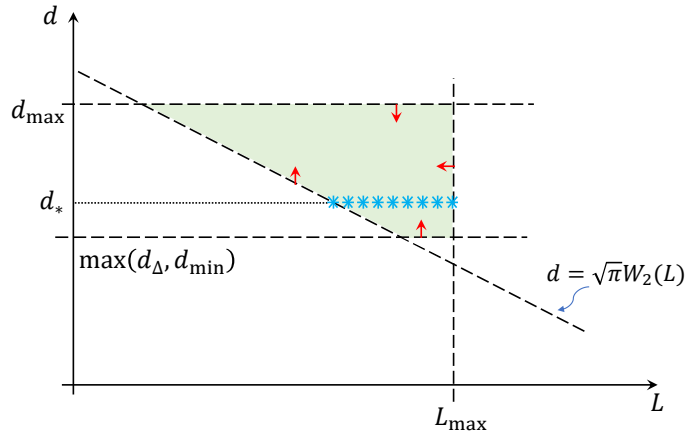$$d \geq d_\Delta \triangleq (A_x \gamma_{\text{req}})^{\frac{1}{3}}, \tag{35}$$

Fig. 9: One example of possible solutions for optimization problem given in (28).

TABLE III: Optimum d for the first optimization problem of DCO-OFDM.

Condition	Optimum d	Optimum L	Behavior of $R(d)$
$d_* < \max(d_\Delta, d_{\min})$	$\max(d_\Delta, d_{\min})$	$[\mathcal{L}(\max(d_\Delta, d_{\min})), L_{\max}]$	decreasing
$\max(d_\Delta, d_{\min}) < d_* < d_{\max}$	d_*	$[\mathcal{L}(d_*), L_{\max}]$	increasing till d_* then decreasing
$d_* > d_{\max}$	$d_{\max}$	$[\mathcal{L}(d_{\max}), L_{\max}]$	increasing

and the third constraint enforces $d \geq d_{\min}$. Therefore, these two apply the condition $d \geq \max(d_\Delta, d_{\min})$. Fig. 9 shows an example of the feasible region of the problem 1 defined by the constraints in (28). The red arrows indicate the direction of feasibility for each boundary curve defined by different constraints in (28). For instance, the region of interest for the condition $d \leq d_{\max}$ is shown with the downward arrow. The blue stars show the maximum points of R. If $\max(d_\Delta, d_{\min}) < d_* < d_{\max}$ as shown in the figure, the function R is maximized at $d_{\text{opt},1} = d_*$. However, if $d_* < \max(d_\Delta, d_{\min})$, R is a decreasing function w.r.t d in the feasible region and the optimum d is $d_{\text{opt},1} = \max(d_\Delta, d_{\min})$. Otherwise, if $d_* > d_{\max}$, R is an increasing function w.r.t d, and therefore, R is maximized at $d_{\text{opt},1} = d_{\max}$. These cases are summarized in Table III. As can be seen from Fig. 9, the optimum L can be from the cross-section of line $d = \sqrt{\pi} W_2(L)$ and $d = d_{\text{opt},1}$ to $L_{\max}$, i.e., in the range $[\mathcal{L}(d_{\text{opt},1}), L_{\max}]$, where $\mathcal{L}(\cdot)$ is given by:

$$\mathcal{L}(x) = f_b - \frac{1}{b_1}\left(\frac{1}{\sqrt{\pi}}x - b_0\right). \tag{36}$$

Optimization problem 2: The objective function of (29) is given by:

$$R = \frac{\nu}{C_t d} \log_2\left(1 + \frac{d^5}{\pi W_2^2(L)\Gamma A_x}\right), \tag{37}$$

which is a function of both d and L. For any L, the function in (37) has a unique maximum at:

$$d_{**}(L) = \left(142.32\pi W_2^2(L)\Gamma A_x\right)^{\frac{1}{5}}. \tag{38}$$
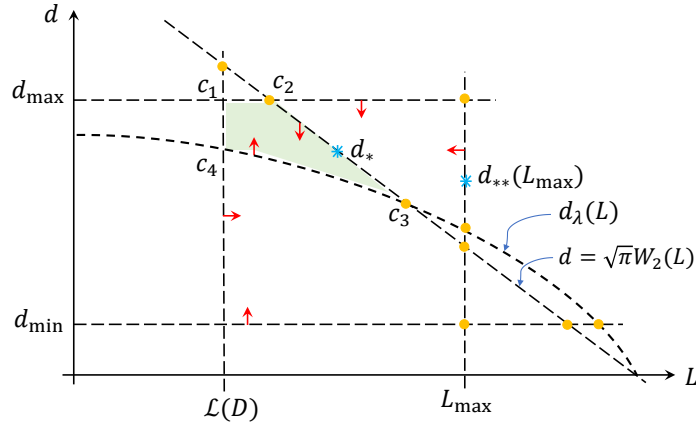
Fig. 10: One example of possible solutions for optimization problem given in (29).

Moreover, the objective function in (37) is an increasing function w.r.t L, for any d. This implies that the solution should be always on the boundary of the feasible region since for any internal point, there exists a point on the boundary of the feasible region with the same d and a higher value of L, which results in a higher R. Fig. 10 represents one example of the feasible region of the problem 2 imposed by the constraints of (29). The possible solutions would be either one of the corner points (shown as yellow circles) or a extremum point that maximize R on a boundary curve (shown as blue stars). The curve $d_\lambda(L)$ shows the boundary of the second constraint of (29) where:

$$d_\lambda(L) \triangleq \left(\pi W_2^2(L) A_x \gamma_{\mathrm{req}} \right)^{\frac{1}{5}}. \tag{39}$$

Note that inserting this curve in the objective function makes R to become independent of L and decreasing w.r.t d with no extremum point. By inserting the fourth constraint of (29) (i.e., $W_2(L) = \frac{d}{\sqrt{\pi}}$) in (37), the objective function simplifies into the objective function of problem 1 given by (33) and therefore, it can be maximized at d_* as in (34). In addition, the 5th constraint of (29) imposes the lower bound $L \geq \mathcal{L}(D)$. Note that most of the corner points on this boundary line do not produce a possible solution. There would exist points with larger L in the feasible region. For the example shown in Fig. 10, d_* is the optimum solution. If d_* was out of the feasible region, then c_2 (or c_3) may be the optimum solution if R is an increasing (or decreasing) function. The possible corner and extremum points are given in Table IV. Therefore, the solution of problem 2 can be determined by finding the optimum point among these possible solutions that satisfy all the constraints.

Optimization problem 3: The objective function of (30) can be expressed as:

$$R = \frac{\nu}{C_{\mathrm{t}} d} \log_2 \left(1 + \frac{D^2 d^5}{\pi^2 W_4^2(L) \Gamma A_x} \right). \tag{40}$$

TABLE IV: Possible optimum solutions for (d, L) for the second optimization problem of DCO-OFDM.

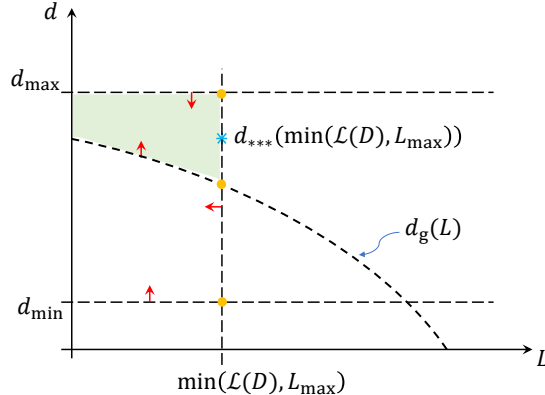| Possible optimum solutions for (d, L)		
$(d_{\max}, L_{\max})$	$(d_{\min}, \mathcal{L}(d_{\min}))$	$(D, \mathcal{L}(D))$
$(d_\lambda(L_{\max}), L_{\max})$	$(d_{\min}, \mathcal{L}(\sqrt{\frac{d_{\min}^5}{A_x \gamma_{\mathrm{req}}}}))$	$(d_*, \mathcal{L}(d_*))$
$(\sqrt{\pi} W_2(L_{\max}), L_{\max})$	$(d_\Delta, \mathcal{L}(d_\Delta))$	$(d_{**}(L_{\max}), L_{\max})$

Fig. 11: One example of possible solutions for optimization problem given in (30).

This function has a similar behavior to the objective function of problem 2 in (37) with a unique maximum point for any L at:

$$d_{***}(L) = \left(\frac{142.32 \pi^2 W_2^4(L) \Gamma A_x}{D^2} \right)^{\frac{1}{5}}. \tag{41}$$

The objective function is also increasing w.r.t to L for any d. Therefore, the solution lies again on the boundary of the feasible region. Fig. 11 illustrates one example of the feasible region imposed by the constraints of (30). The curve labeled as $d_{\mathrm{g}}(L)$ is the boundary condition imposed by the second constraint in (30) where:

$$d_{\mathrm{g}}(L) \triangleq \left(\pi^2 W_2^4(L) \frac{A_x}{D^2} \gamma_{\mathrm{req}} \right)^{\frac{1}{5}}. \tag{42}$$

Note that inserting $d_{\mathrm{g}}(L)$ in the objective function (40), makes R a decreasing function of d and independent of L with no extremum. In addition, based on the first and fourth constraints of (30), $L \leq \min(\mathcal{L}(D), L_{\max})$. Therefore, the possible solutions are either the extremum or the corner points on the upper boundary of L as shown in Fig. 11. Table V summarizes different conditions under which any of these points would be the solution of problem 3.

The global optimal solution of DCO-OFDM can be then obtained based on the optimum solution of each optimization problem, i.e., the one that results in the maximum data rate.

TABLE V: Optimum d for the third optimization problem of DCO-OFDM. The optimum L is $\min(\mathcal{L}(D), L_{\max})$ for all optimum d's.

Condition	Optimum d
$d_{***}(\min(\mathcal{L}(D), L_{\max})) < \max(d_{\min}, d_{\mathrm{g}}(\min(\mathcal{L}(D), L_{\max})))$	$\max(d_{\min}, d_{\mathrm{g}}(\min(\mathcal{L}(D), L_{\max})))$
$\max(d_{\min}, d_{\mathrm{g}}(\min(\mathcal{L}(D), L_{\max}))) < d_{***}(\min(\mathcal{L}(D), L_{\max})) < d_{\max}$	$d_{***}(\min(\mathcal{L}(D), L_{\max}))$
$d_{***}(\min(\mathcal{L}(D), L_{\max})) > d_{\max}$	$d_{\max}$

B. OOK Modulation

The data rate of OOK modulation is limited by the Nyquist's sampling rate, i.e., $R \leq 2B$. Although this requires employing efficient pulse shaping techniques, experimental studies have shown that data rates close to the Nyquist limit are achievable for OOK modulation [59]–[61]. The linear relationship between R and B, indicates that B can replace R as the objective function of the optimization problem in (28), (29) and (30) for OOK modulation. Furthermore, replacing (2) for B, we have:

$$R = \frac{2}{C_{\mathrm{t}} d}. \tag{43}$$

Note that the objective function is a monotonically decreasing function of d and does not depend on L; hence the maximized solution should happen at the boundary of the feasible set, i.e., at the minimum value of d. Next, we find the optimum (i.e., minimum) d within the feasible set of the three optimization problem given in (28)-(30).

Optimization problem 1: Similar to the first optimization problem of DCO-OFDM, the second and third constraints of (28) implies $d \geq \max(d_{\Delta}, d_{\min})$, where d_{Δ} is defined in (35). Since $W_2(L)$ is a decreasing function of L, inserting $L = L_{\max}$ in (28e) gives a lower limit on the value of d. Therefore, considering the lower bounds defined by the second, third, and fourth constraints in (28), the optimum (i.e., minimum) value of d can be expressed as:

$$d_{\mathrm{opt},1} = \max\left(d_{\min}, d_{\Delta}, \sqrt{\pi} W_2(L_{\max})\right), \tag{44}$$

for $\max\left(d_{\Delta}, \sqrt{\pi} W_2(L_{\max})\right) \leq D\sqrt{\frac{\mathrm{FF}}{N_{\mathrm{PD}}}}$; otherwise this condition does not provide a solution. Also note that L should be taken from $[\mathcal{L}(d_{\mathrm{opt},1}), L_{\max}]$.

Optimization problem 2: The second constraint of (29) indicates $d \geq d_{\lambda}(L)$, where $d_{\lambda}(L)$ is given in (39). Noting that $d_{\lambda}(L)$ is a decreasing function of L, the minimum value of d (to ensure maximum data rate) can be obtained on the boundary of feasible set at the maximum possible value of L. The maximum L may be either on the line $L = L_{\max}$ or on the cross-section of the lines $d = \sqrt{\pi} W_2(L)$ and $d_{\lambda}(L)$ (see Fig. 10). It can be shown that the cross-section of the two lines happens at $L = \mathcal{L}((A_x \gamma_{\mathrm{req}})^{\frac{1}{3}})$. Therefore, the optimum value of L is

TABLE VI: The possible solutions of the optimization problem for OOK.

Optimum L	Optimum d
$[L_\Delta, L_{\max}]$	$d_{\mathrm{opt},1} = \max\left(d_{\min}, d_\Delta, \sqrt{\pi}W_2(L)\right)$
$\min(\mathcal{L}((A_x\gamma_{\mathrm{req}})^{\frac{1}{3}})), L_{\max})$	$d_{\mathrm{opt},2} = \max\left(d_{\min}, d_\lambda(\min(\mathcal{L}((A_x\gamma_{\mathrm{req}})^{\frac{1}{3}})), L_{\max})))\right)$
$\min(\mathcal{L}(D), L_{\max})$	$d_{\mathrm{opt},3} = \max\left(d_{\min}, d_{\mathrm{g}}(\min(\mathcal{L}(D), L_{\max})))\right)$

$\min(\mathcal{L}((A_x\gamma_{\mathrm{req}})^{\frac{1}{3}})), L_{\max})$. Applying the third constraint in (29), the solution for d is given by:

$$d_{\mathrm{opt},2} = \max\left(d_{\min}, d_\lambda(\min(\mathcal{L}((A_x\gamma_{\mathrm{req}})^{\frac{1}{3}})), L_{\max}))\right), \tag{45}$$

for $d_{\lambda,\min} \leq D\sqrt{\frac{\mathrm{FF}}{N_{\mathrm{PD}}}}$; otherwise this condition does not provide a solution.

Optimization problem 3: The second constraint of this optimization problem gives $d \geq d_{\mathrm{g}}(L)$ where $d_{\mathrm{g}}(L)$ is defined in (42). Based on the first and fourth constraints of (30), $L \leq \min(\mathcal{L}(D), L_{\max})$. Similarly, $d_{\mathrm{g}}(L)$ is a decreasing function of L; hence, the minimum value of d is achieved on the boundary of feasible set at the maximum value of L. Similarly, by applying the third constraint in (30), the solution for d is obtained as:

$$d_{\mathrm{opt},3} = \max\left(d_{\min}, d_{\mathrm{g}}(\min(\mathcal{L}(D), L_{\max}))\right). \tag{46}$$

for $d_{\mathrm{g}}(\min(\mathcal{L}(D), L_{\max})) \leq D\sqrt{\frac{\mathrm{FF}}{N_{\mathrm{PD}}}}$; otherwise this condition does not provide a solution.

The solutions of these three optimization problems are outlined in Table VI. The global optimal solution of OOK can be then obtained based on the minimum value of (44), (45) and (46).

V. SIMULATION RESULTS

A single mode vertical cavity surface emitting laser (VCSEL) transmitter is considered which operates at 850 nm with a beam waist of 5 μm. A lens is placed in front of the VCSEL source to produce a 20 cm beam spot diameter at 2 m. The transmit power of 10 mW is obtained based on the eye safety considerations [58], which enforces a power-limited regime. The maximum size of receiver is set to be 2 cm $\times$ 2 cm. The FF of the array is set to $\mathrm{FF} = 0.64$ similar to the fabricated array in [36]. We have fixed the size of each inner array to 400 μm $\times$ 400 μm (similar to [36]). Each inner array is equipped with the aspheric lens $354140-$B from Thorlabs[3]. The lens parameters are provided in Table I. We have also evaluated the transmission coefficient of the considered aspheric lens using OpticStudio by calculating the ratio between the transmission power through the lens and its incident power. The results show that the transmission coefficient is $\xi_{\mathrm{r}} = 0.88$. The rest of the simulation parameters are provided in Table VII.

---

[3]This lens is just an example and other lenses can be also used.

TABLE VII: Simulation Parameters.

Parameter	Symbol	Value
Feedback resistor	R_f	500 Ω
Load resistor	R_L	50 Ω
Junction series resistor	R_s	7 Ω [47]
Carrier saturation velocity	v_s	4.8×10^4 m/s
TIA noise figure	F_n	5 dB
Temperature	T	300° K
Side length of inner array	D	400 μm
Transmission coefficient	ξ_r	0.88
Transmit power	P_t	10 mW
Receiver responsivity	R_res	0.5 A/W
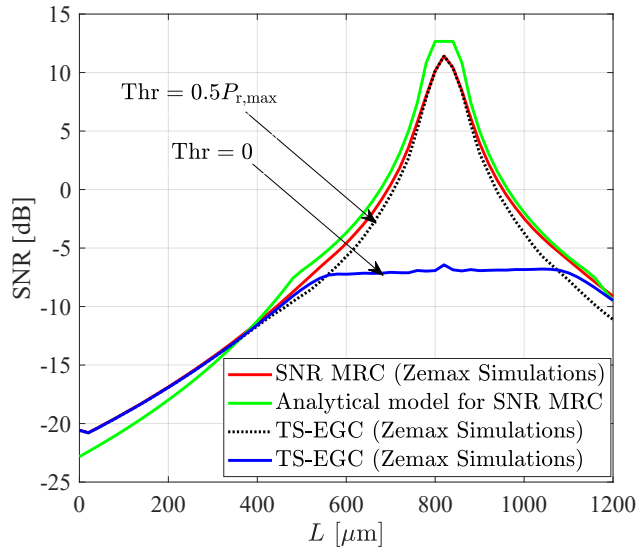
Fig. 12: SNR versus L for MRC, TS-EGC and the analytical model based on (22) for $\mathcal{N}_\mathrm{a} = 64$ and $N_\mathrm{PD} = 64$.

Fig. 12 illustrates the SNR results of MRC and TS-EGC obtained from OpticStudio. The results are shown for $\mathcal{N}_\mathrm{a} = 64$ and $N_\mathrm{PD} = 49$. Two thresholds of 0 and $0.5P_\mathrm{r,max}$ are considered for TS-EGC, where $P_\mathrm{r,max}$ is the maximum received power of PDs on an array. When $\mathrm{Thr} = 0$, the performance of TS-EGC is exactly the same as traditional EGC (blue curve). As it can be seen, the TS-EGC with $\mathrm{Thr} = 0.5P_\mathrm{r,max}$ has a similar performance as MRC. In Fig. 12, the analytical expression for the SNR of MRC given in (25) is compared with the simulation results, which proves the accuracy of our analytical model. Hence one can rely on the proposed analytical model instead of OpticStudio ray-tracing simulations to save computation time.

We now present the results of optimization problem for DCO-OFDM, where the number of subcarriers is set to 512. Fig. 13a-c illustrate the feasible regions for $\gamma \geq \gamma_\mathrm{req} = 10.6$ (this ensures $\mathrm{BER} \leq \mathrm{BER}_\mathrm{req} = 0.001$ for DCO-OFDM [16]) and $\mathrm{FOV} \geq \mathrm{FOV}_\mathrm{req} = 15°$ (or equivalently for $L \leq 820$ μm based on (9)), when $\mathcal{N}_\mathrm{a} = 64$, $N_\mathrm{PD} = 36$ and $\mathrm{FF} = 0.64$. The cyan areas
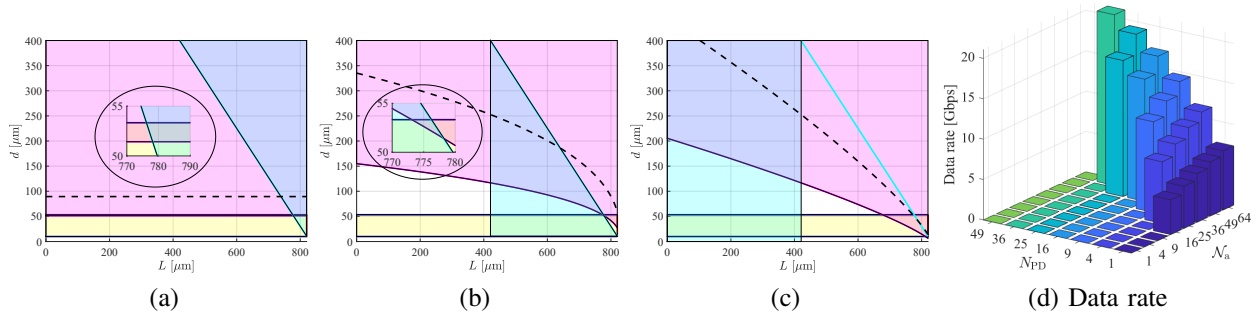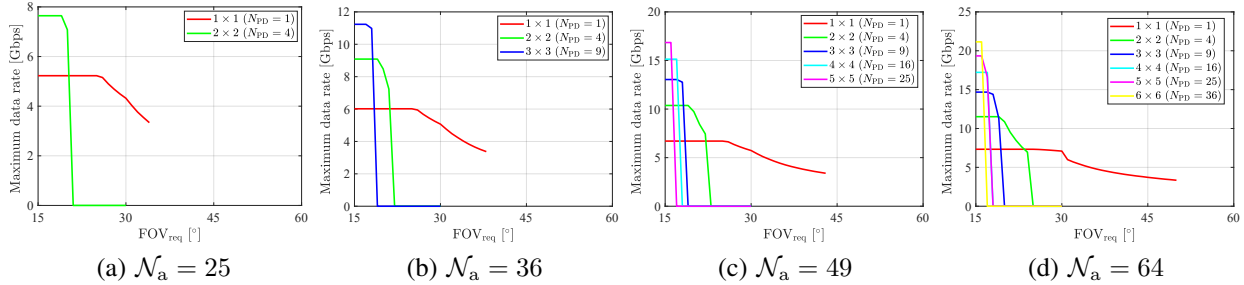
Fig. 13: Feasible region based on (a) first, (b) second and (c) third equations of SNR given in (25).

(a) $\mathcal{N}_{\mathrm{a}} = 25$ (b) $\mathcal{N}_{\mathrm{a}} = 36$ (c) $\mathcal{N}_{\mathrm{a}} = 49$ (d) $\mathcal{N}_{\mathrm{a}} = 64$

Fig. 14: Maximum data rate versus $\mathrm{FOV}_{\mathrm{req}}$ for different number of PDs on a single array and different sizes of array of arrays. DCO-OFDM and FF of 0.64 are assumed for these results.

correspond to each sub-function of (25). The magenta areas represent the conditions given in (35), (39) and (42). These conditions guarantee the required SNR. The yellow areas indicate the third constraint in (23), which is $10 \ \mu\mathrm{m} \leq d \leq 400\sqrt{\frac{0.64}{36}} = 53.33 \ \mu\mathrm{m}$. The feasible region for each optimization problem can be found by looking into the intersection of different areas in each figure. It can be seen that there is no intersections between the areas in Fig. 13c. However, the first equation of SNR in (25) yields a nonempty feasible region as shown in Fig. 13a. There are plenty of combinations for the pair of (d, L) that fulfill $\mathrm{BER} \leq 0.001$ and $\mathrm{FOV} \geq 15$. The optimum one that maximizes R can be determined based on the third row of Table III. Since $R(d)$ is a monotonically increasing function in the range of $d \in [d_{\min}, d_{\max}]$, $d_{\mathrm{opt}} = d_{\max} = 53.33 \ \mu\mathrm{m}$. Furthermore, $L_{\mathrm{opt}} \in [777, 820] \ \mu\mathrm{m}$, where the choice of $L = 777 \ \mu\mathrm{m}$ yields the FOV of $16.4°$. Fig. 13d presents the achievable data rate versus N_{PD} in each inner array and $\mathcal{N}_{\mathrm{a}}$. A maximum data rate of 21.14 Gbps can be achieved for the given BER of 0.001 and the FOV of $15°$ using DCO-OFDM. It is also assumed that the maximum size of the receiver is $2 \ \mathrm{cm} \times 2 \ \mathrm{cm}$ in these results. The inner array that provides the maximum data rate includes 6×6 PDs ($N_{\mathrm{PD}} = 36$) with side length of $53.33 \ \mu\mathrm{m}$. This size of a PD provides a bandwidth of 10 GHz and it ensures the BER is less than 0.001. A minimum of $\mathcal{N}_{\mathrm{a}} = 16$ arrays is required to guarantee the desired BER of 0.001 and the required FOV of $15°$, which achieves data rate of 4.3 Gbps.

Fig. 14 indicates the maximum data rate versus the required FOV for DCO-OFDM. The rate-FOV trade-off can be observed in these results. Each subfigure represents a specific $\mathcal{N}_a$. It should be noted that none of the receiver structures with $\mathcal{N}_a = 1$, $\mathcal{N}_a = 4$ and $\mathcal{N}_a = 9$ are able to fulfill the BER and FOV requirements. A receiver with $\mathcal{N}_a = 16$ arrays can ensure the design requirements, only if each inner array includes 1 PD. As shown in Fig. 14a, a receiver that includes $\mathcal{N}_a = 25$ arrays with either $N_{PD} = 1$ or $N_{PD} = 4$ structure for the inner arrays can ensure the desired BER and FOV. The inner array with $N_{PD} = 4$ PDs support higher data rate and lower FOV compared to the one with $N_{PD} = 1$ structure. When the size of the receiver increases to $\mathcal{N}_a = 64$ arrays, each inner array with 1 PD upto 36 PD arrangement are able to support BER of less than 0.001 and the required FOV. The maximum data rate is related to $\mathcal{N}_a = 64$ arrays with $N_{PD} = 36$ PDs on each inner array, which is 21.14 Gbps. These maximum data rate can be achieved for $777 \leq L \leq 820$ μm.

Next, we present the results for OOK. Fig. 15 illustrates these feasible regions for optimization problems given in (28), (29) and (30) for $\gamma \geq \gamma_{req} = 9.55$ and FOV $\geq$ FOV$_{req} = 15°$, when $\mathcal{N}_a = 64$, $N_{PD} = 49$ and FF $= 0.64$. The constraint $\gamma \geq \gamma_{req} = 9.55$ ensures BER $\leq$ BER$_{req} = 10^{-3}$ for the OOK modulation [18]. The yellow areas indicate the third constraint in (23), which is 10 μm $\leq d \leq 400\sqrt{\frac{0.64}{49}} = 45.7$ μm. The feasible region for the optimization problem can be found by looking into the intersection of the areas. The subsets in Fig. 15a and Fig. 15b depict the zoomed intersection areas for convenience. The optimum value of d is the smallest in the intersection area to ensure the maximum data rate since $R = \frac{2}{C_t d}$. Therefore, $d_{opt} = d_\Delta = 44.81$ μm and $L_{opt} \in [785, 820]$ μm, which are in agreement with the analytical solutions given in first row of the Table VI for OOK modulation. We note that the choice of $L = 785$ μm results in the FOV of $16.2°$. Fig. 15d presents the achievable data rate versus the number of PDs in each inner array and the number of arrays. A maximum data rate of 23.82 Gbps can be achieved for a given BER of 10^{-3} and a FOV of $15°$ using OOK modulation. It is assumed that the maximum length of the receiver is 2 cm in these results. The inner array that provides the maximum data rate includes 7×7 PDs each with a side length of 44.81 μm. This size of a PD provides a bandwidth of 11.91 GHz and it ensures the BER is less than 10^{-3}. The achieved FF of the array is 0.61 which is very close to our target FF of 0.64. A minimum of $\mathcal{N}_a = 9$ is required to fulfill the required BER of 10^{-3} and the required FOV of $15°$, which achieves data rate of 3.38 Gbps. It can be also observed that when the number of PDs (N_{PD}) increases, a bigger size of receiver (i.e., larger $\mathcal{N}_a$) is also required to satisfy the BER and FOV requirements. This is due the higher
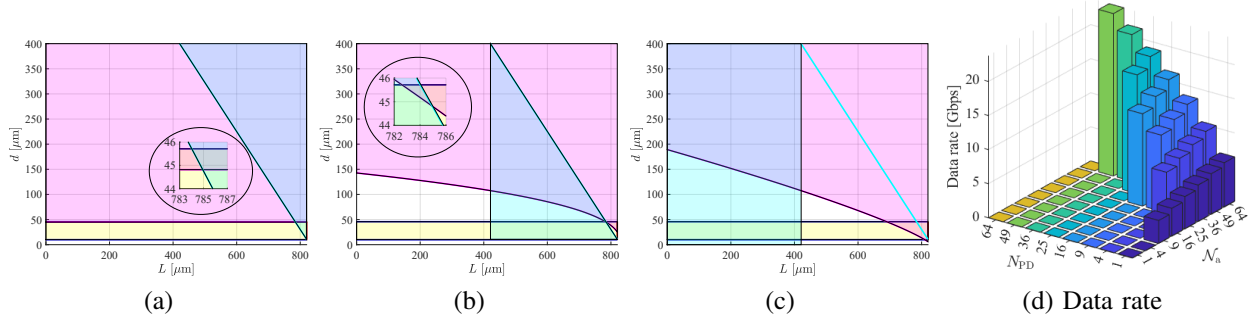
Fig. 15: Feasible region based on (a) first, (b) second and (c) third equations of SNR given in (25).
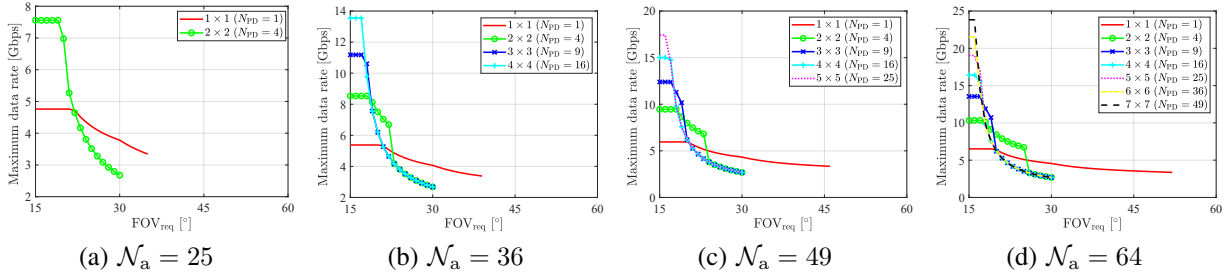

Fig. 16: Maximum data rate versus FOV_{req} for different number of PDs on the inner array and different values of $\mathcal{N}_a$. OOK modulation and FF of 0.64 are assumed for these results.

thermal noise accumulated in a larger PD array.

Fig. 16 shows the maximum data rate versus the required FOV. Each subfigure represents a specific size of receiver (indicated by the number of outer arrays, $\mathcal{N}_a$). We note that neither $\mathcal{N}_a = 1$ nor $\mathcal{N}_a = 4$ are able to fulfill the BER and FOV requirement. Both sizes of $\mathcal{N}_a = 9$ and $\mathcal{N}_a = 16$ can ensure the design requirements, only if $N_{PD} = 1$. A receiver with $\mathcal{N}_a = 25$ with either $N_{PD} = 1$ or $N_{PD} = 4$ configuration is able to guarantee BER of less than 0.001 and required FOV of $15°$ as shown in Fig. 16a. The rate-FOV trade-off can be observed in these results, where higher data rate are achievable in cost of lower FOV. For $\mathcal{N}_a = 25$, the PD configuration with $N_{PD} = 4$ is able to fulfill $FOV_{req} \leq 30°$ while the PD configuration with $N_{PD} = 1$ can support $FOV_{req} \leq 35°$. As shown in Fig. 16d, when $\mathcal{N}_a$ increases to 64, inner arrays with N_{PD} up to 49 detectors are able to support the desired BER and FOV. The maximum data rate is related to the receiver structure with $\mathcal{N}_a = 64$ and $N_{PD} = 49$, which is 23.82 Gbps. These maximum data rate can be achieved for $785 \leq L \leq 820$ μm. It worth mentioning that inner arrays with $N_{PD} \geq 64$ are not able to satisfy the BER requirement. The reason is that the high bandwidth of the PDs adds more noise to the system. This is in accordance with the early statement that choosing high bandwidth PDs in a power-limited regime is not helpful as more noise will be added to the system. It is also noted that $FOV \geq 30°$ can be achieved only with

single-PD arrays at very close distances to the lens. Arrays with other PD configurations fail to assure $\text{BER} \leq 0.001$. For a single PD equal to the size of the array ($400 \times 400 \ \mu\text{m}^2$), we can attain $70°$ FOV at $L \approx 0$ (see Fig. 5d) and a maximum data rate of 2.68 Gbps with $\mathcal{N}_\text{a} = 64$. It should be highlighted that we are in a power-limited regime due to eye safety considerations, where lower modulations order are preferable. That is the reason, OOK outperforms DCO-OFDM. However, in a high SNR regime (which can be realized with APD), DCO-OFDM should be able to outperform OOK.

VI. Summary and Concluding Remarks

In this study, we proposed a design of high-speed imaging receiver that can support mobility based on an array of arrays structure to address the two well-known optical design trade-offs, i.e., area-bandwidth and gain-FOV trade-offs. The proposed receiver is able to control the combined impacts of both trade-offs effectively achieving the best receiver performance that is constrained by a rate-FOV trade-off. We derived the analytical model of SNR for the proposed array of arrays structure. The analytical models are verified with realistic simulations conducted in OpticStudio (Zemax) software. We then formulated an optimization problem to assure design requirements such as FOV and BER for OOK modulation and DCO-OFDM. Furthermore, we derived the optimum side length of PDs and the distance between an array and the lens to maximize the achievable data rate of the system. In order to have realistic simulations, we considered practical aspects of the receiver elements, such as the transmission coefficient of the lens, etc. The simulations of beam intensity profile and SNR are carried out using the OpticStudio software, which ensures the reliability of our results. Insightful results and in-depth discussions are demonstrated for both OOK and DCO-OFDM. Simulation results confirm that with a square lattice arrangement of 8×8 array of arrays, we are able to achieve a maximum data rate of 23.82 Gbps and 21.14 Gbps data rate with a FOV of $15°$ using OOK and DCO-OFDM, respectively. Some possible directions for future research can be the use of a non-imaging structure, angle diversity receiver formation and selection combining technique.

VII. Acknowledgement

Appendix

The derivative of (33) w.r.t d is given as:

$$\frac{\partial}{\partial d}\left(\frac{\nu}{C_{\mathrm{t}} d}\log_2\left(1+\frac{d^3}{\Gamma A_x}\right)\right)=\frac{\nu}{C_{\mathrm{t}}}\frac{\dfrac{\dfrac{3d^3}{\Gamma A_x}}{\dfrac{d^3}{\Gamma A_x}+1}-\ln\left(\dfrac{d^3}{\Gamma A_x}+1\right)}{d^2\ln(2)}. \tag{47}$$

Let us define the auxiliary variable $\varphi \triangleq \frac{d^3}{\Gamma A_x}+1$, we need to find the roots of $3(\varphi-1)-\varphi\ln(\varphi)=0$, which are $\varphi_1 = 1$ and $\varphi_2 = \exp\left(\Phi(-3/e^3)+3\right) = 16.8$, where $\Phi(x)$ is the product logarithm function (also known as Lambert W-function), which is the inverse function of $f(x) = xe^x$. Therefore, the roots of (47) are $d = 0$ and $d = (15.8\Gamma A_x)^{\frac{1}{3}} \triangleq d_*$. The derivation given in (47) is negative for $d < 0$, positive for $d \in (0, d_*)$ and negative for $d > d_*$. Hence, $d = 0$ is a minimum and $d = d_*$ is a maximum of R given in (33), respectively.

References

[1] M. D. Soltani, H. Kazemi, E. Sarbazi, H. Haas, and M. Safari, "Optimal Imaging Receiver Design for High-Speed Mobile Optical Wireless Communications," in *2022 7th IEEE ICC Workshop on Optical Wireless Communications (OWC'22)*, 2022, pp. 1–6.

[2] Cisco white paper. (2020, Mar.) Annual Internet Report (2018–2023). [Online]. Available: https://www.cisco.com/c/en/us/solutions/collateral/executive-perspectives/annual-internet-report/white-paper-c11-741490.html

[3] "Cisco Annual Internet Report (2018–2023) White Paper," Cisco, Tech. Rep., Mar. 2020.

[4] M. A. Khalighi and M. Uysal, "Survey on Free Space Optical Communication: A Communication Theory Perspective," *IEEE Communications Surveys Tutorials*, vol. 16, no. 4, pp. 2231–2258, 2014.

[5] D. Karunatilaka, F. Zafar, V. Kalavally, and R. Parthiban, "Led based indoor visible light communications: State of the art," *IEEE Communications Surveys & Tutorials*, vol. 17, no. 3, pp. 1649–1678, 2015.

[6] Z. Zeng, S. Fu, H. Zhang, Y. Dong, and J. Cheng, "A survey of underwater optical wireless communications," *IEEE Communications Surveys Tutorials*, vol. 19, no. 1, pp. 204–238, 2017.

[7] S. Teli, W. A. Cahyadi, and Y. H. Chung, "Optical camera communication: Motion over camera," *IEEE Communications Magazine*, vol. 55, no. 8, pp. 156–162, 2017.

[8] H. Haas, L. Yin, Y. Wang, and C. Chen, "What is LiFi?" *J. Lightw. Technol.*, vol. 34, no. 6, pp. 1533–1544, 2016.

[9] H. Haas, J. Elmirghani, and I. White, "Optical wireless communication," *Philosophical Transactions of the Royal Society A: Mathematical, Physical and Engineering Sciences*, vol. 378, no. 2169, p. 20200051, 2020.

[10] T. Koonen, "Indoor Optical Wireless Systems: Technology, Trends, and Applications," *Journal of Lightwave Technology*, vol. 36, no. 8, pp. 1459–1467, Apr. 2018.

[11] H. Elgala, R. Mesleh, and H. Haas, "Indoor Optical Wireless Communication: Potential and State-of-the-Art," *IEEE Commun. Mag.*, vol. 49, no. 9, pp. 56–62, Sep. 2011.

[12] Y. Hong, F. Feng, K. R. H. Bottrill, N. Taengnoi, R. Singh, G. Faulkner, D. C. O'Brien, and P. Petropoulos, "Demonstration of > 1 Tbit/s WDM OWC with wavelength-transparent beam tracking-and-steering capability," *Opt. Express*, vol. 29, no. 21, pp. 33 694–33 702, Oct 2021.

[13] R. Singh, F. Feng, Y. Hong, G. Faulkner, R. Deshmukh, G. Vercasson, O. Bouchet, P. Petropoulos, and D. O'Brien, "Design and characterisation of terabit/s capable compact localisation and beam-steering terminals for fiber-wireless-fiber links," *Journal of Lightwave Technology*, vol. 38, no. 24, pp. 6817–6826, 2020.

[14] T. Koonen, K. Mekonnen, Z. Cao, F. Huijskens, N. Q. Pham, and E. Tangdiongga, "Ultra-high-capacity wireless communication by means of steered narrow optical beams," *Philosophical Transactions of the Royal Society A: Mathematical, Physical and Engineering Sciences*, vol. 378, no. 2169, p. 20190192, 2020.

[15] E. Sarbazi, H. Kazemi, M. D. Soltani, M. Safari, and H. Haas, "A Tb/s Indoor Optical Wireless Access System Using VCSEL Arrays," in *2020 IEEE 31st Annual International Symposium on Personal, Indoor and Mobile Radio Communications*, 2020, pp. 1–6.

[16] H. Kazemi, E. Sarbazi, M. D. Soltani, M. Safari, and H. Haas, "A Tb/s Indoor Optical Wireless Backhaul System Using VCSEL Arrays," in *2020 IEEE 31st Annual International Symposium on Personal, Indoor and Mobile Radio Communications*, 2020, pp. 1–6.

[17] J. Chaves, *Introduction to Nonimaging Optics*. CRC press, 2008.

[18] J. M. Kahn and J. R. Barry, "Wireless Infrared Communications," *Proceedings of the IEEE*, vol. 85, no. 2, pp. 265–298, 1997.

[19] O. Alkhazragi, A. Trichili, I. Ashry, T. K. Ng, M.-S. Alouini, and B. S. Ooi, "Wide-field-of-view optical detectors using fused fiber-optic tapers," *Opt. Lett.*, vol. 46, no. 8, pp. 1916–1919, Apr 2021.

[20] T. Q. Wang, C. He, and J. Armstrong, "Performance Analysis of Aperture-Based Receivers for MIMO IM/DD Visible Light Communications," *Journal of Lightwave Technology*, vol. 35, no. 9, pp. 1513–1523, 2017.

[21] C. He, T. Q. Wang, and J. Armstrong, "Performance of Optical Receivers Using Photodetectors With Different Fields of View in a MIMO ACO-OFDM System," *Journal of Lightwave Technology*, vol. 33, no. 23, pp. 4957–4967, 2015.

[22] S. Collins, D. C. O'Brien, and A. Watt, "High Gain, Wide Field of View Concentrator for Optical Communications," *Opt. Lett.*, vol. 39, no. 7, pp. 1756–1759, Apr 2014.

[23] A. Riaz, G. Faulkner, and S. Collins, "A Fluorescent Antenna for White Light Visible Light Communications," in *2019 Global LIFI Congress (GLC)*, 2019, pp. 1–4.

[24] P. P. Manousiadis, S. Rajbhandari, R. Mulyawan, D. A. Vithanage, H. Chun, G. Faulkner, D. C. O'Brien, G. A. Turnbull, S. Collins, and I. D. Samuel, "Wide Field-of-View Fluorescent Antenna for Visible Light Communications Beyond the étendue Limit," *Optica*, vol. 3, no. 7, pp. 702–706, Jul 2016.

[25] S. B. Alexander, *Optical Communication Receiver Design*. Bellingham: SPIE Press, 1997.

[26] O. Kharraz and D. Forsyth, "Performance comparisons between pin and apd photodetectors for use in optical communication systems," *Optik*, vol. 124, no. 13, pp. 1493–1498, 2013.

[27] S. D. Personick, "Receiver design for digital fiber optic communication systems, i," *Bell system technical journal*, vol. 52, no. 6, pp. 843–874, 1973.

[28] S. Bashiri, C. Plett, J. Aguirre, and P. Schvan, "A 40 gb/s transimpedance amplifier in 65 nm cmos," in *Proceedings of 2010 IEEE International Symposium on Circuits and Systems*, 2010, pp. 757–760.

[29] S. G. Kim, C. Hong, Y. S. Eo, J. Kim, and S. M. Park, "A 40-ghz mirrored-cascode differential transimpedance amplifier in 65-nm cmos," *IEEE Journal of Solid-State Circuits*, vol. 54, no. 5, pp. 1468–1474, 2019.

[30] I. G. López, A. Awny, P. Rito, M. Ko, A. Ulusoy, and D. Kissinger, "A 60 GHz bandwidth differential linear TIA in 130 nm sige:C BiCMOS with lt; 5.5 pA/$\sqrt{\text{Hz}}$," in *2017 IEEE Bipolar/BiCMOS Circuits and Technology Meeting (BCTM)*, 2017, pp. 114–117.

[31] I. Garcia López, A. Awny, P. Rito, M. Ko, A. C. Ulusoy, and D. Kissinger, "100 Gb/s Differential Linear TIAs With Less Than 10 pA/ $\sqrt{\text{Hz}}$ in 130-nm SiGe:C BiCMOS," *IEEE Journal of Solid-State Circuits*, vol. 53, no. 2, pp. 458–469, 2018.

[32] K. Vasilakopoulos, S. P. Voinigescu, P. Schvan, P. Chevalier, and A. Cathelin, "A 92ghz bandwidth sige bicmos hbt tia with less than 6db noise figure," in *2015 IEEE Bipolar/BiCMOS Circuits and Technology Meeting - BCTM*, 2015, pp. 168–171.

[33] M. S. Bashir, "Free-space optical communications with detector arrays: A mathematical analysis," *IEEE Transactions on Aerospace and Electronic Systems*, vol. 56, no. 2, pp. 1420–1429, 2020.

[34] M.-C. Tsai, M. S. Bashir, and M.-S. Alouini, "A single detector versus an array of detectors receiver in free-space optical communications: A performance comparison," 2021.

[35] T. Koonen, K. Mekonnen, F. Huijskens, Z. Cao, and E. Tangdiongga, "Novel broadband owc receiver with large aperture and wide field-of-view," in *2020 European Conference on Optical Communications (ECOC)*, 2020, pp. 1–4.

[36] T. Umezawa, A. Matsumoto, K. Akahane, S. Nakajima, and N. Yamamoto, "Large submillimeter high-speed photodetector for large aperture fso receiver," *IEEE Journal of Selected Topics in Quantum Electronics*, vol. 28, no. 2, pp. 1–9, 2022.

[37] V. Vilnrotter and M. Srinivasan, "Adaptive detector arrays for optical communications receivers," *IEEE Transactions on Communications*, vol. 50, no. 7, pp. 1091–1097, 2002.

[38] Y. Chen, Z. Xie, J. Huang, Z. Deng, and B. Chen, "High-speed uni-traveling carrier photodiode for 2μm wavelength application," *Optica*, vol. 6, no. 7, pp. 884–889, Jul 2019.

[39] "LPD3040: 40-Gb/s InGaAs PIN Photodiode," Broadcom. [Online]. Available: https://docs.broadcom.com/doc/LPD3040-PB

[40] T. Umezawa, T. Sakamoto, A. Kanno, N. Yamamoto, and T. Kawanishi, "High speed 2-d photodetector array for space and mode-division multiplexing fiber communications," *Journal of Lightwave Technology*, vol. 36, no. 17, pp. 3684–3692, 2018.

[41] "High Speed Photodetector, 1000-1650 nm Battery Biased InGaAs Detector, 15 GHz," Newport. [Online]. Available: https://www.newport.com/p/818-BB-35

[42] "> 10 GHz Photodetectors," Electro-Optics Technology, Inc. [Online]. Available: https://www.eotech.com/content/userfiles/+10%20GHz.pdf

[43] "1-4Gbps GaAsPIN Photodiode," Global Communication Semiconductors. [Online]. Available: http://www.gcsincorp.com/pdf/optical_chips/GaAs%20PIN/GCS%20GaAs%20PIN%20Do007_100um_PIN4_datasheet%20v4.pdf

[44] "PDIN Series Analog InGaAsP PIN Photodiodes," PD-LD. [Online]. Available: https://www.ushio.com/files/specifications/pd-ld-ingaas-analog-photodiodes-1310-1550.pdf

[45] "InGaAs PIN photodiode: G6854-01," Hamamatsu. [Online]. Available: https://www.hamamatsu.com/resources/pdf/ssd/g6854-01_kird1013e.pdf

[46] "InGaAs PIN photodiode: G11193-02R," Hamamatsu. [Online]. Available: https://www.hamamatsu.com/resources/pdf/ssd/g11193_series_kird1111e.pdf

[47] N. Dupuis, D. M. Kuchta, F. E. Doany, A. Rylyakov, J. Proesel, C. Baks, C. L. Schow, S. Luong, C. Xie, L. Wang, S. Huang, K. Jackson, and N. Y. Li, "Exploring the limits of high-speed receivers for multimode vcsel-based optical links," in *OFC 2014*, 2014, pp. 1–3.

[48] Zemax, "Opticstudio." [Online]. Available: https://www.zemax.com/products/opticstudio

[49] "Unmounted Aspheric Lens:354140-B," Thorlabs. [Online]. Available: https://www.thorlabs.com/newgrouppage9.cfm?objectgroup_id=3811

[50] M. Born and E. Wolf, *Principles of optics: electromagnetic theory of propagation, interference and diffraction of light.* Cambridge University Press, 1999.

[51] B. E. Saleh and M. C. Teich, *Fundamentals of Photonics*, 3rd ed. John Wiley & Sons, Inc., 2019, vol. Part I: Optics.

[52] "Understanding Focal Length and Field of View," Edmund Optics. [Online]. Available: https://www.edmundoptics.co.uk/knowledge-center/application-notes/imaging/understanding-focal-length-and-field-of-view/

[53] R. Winston, J. C. Miñano, P. G. Benitez *et al.*, *Nonimaging optics.* Elsevier, 2005.

[54] H.-J. Choi, C. Cho, S. Woo, J.-Y. Lee, Y.-E. Yoo, M. Jeon, G.-H. Kim, T.-J. Je, and E.-c. Jeon, "Manufacturing of compound parabolic concentrator devices using an ultra-fine planing method for enhancing efficiency of a solar cell," *International Journal of Precision Engineering and Manufacturing-Green Technology*, vol. 8, no. 5, pp. 1405–1414, 2021.

[55] E. Sarbazi, H. Kazemi, M. D. Soltani, M. Safari, and H. Haas, "Design Tradeoffs of Non-Imaging Angle Diversity Receivers for 6G Optical Wireless Access Networks," in *2022 IEEE Global Communications Conference (GLOBECOM)*, 2022, pp. 1–6.

[56] A. Goldsmith, *Wireless communications.* Cambridge university press, 2005.

[57] Z. Ghassemlooy, W. Popoola, and S. Rajbhandari, *Optical wireless communications: system and channel modelling with Matlab®.* CRC press, 2019.

[58] M. D. Soltani, E. Sarbazi, N. Bamiedakis, P. de Souza, H. Kazemi, J. M. H. Elmirghani, I. H. White, R. V. Penty, H. Haas, and M. Safari, "Safety analysis for laser-based optical wireless communications: A tutorial," 2021.

[59] H. Le Minh, D. O'Brien, G. Faulkner, L. Zeng, K. Lee, D. Jung, Y. Oh, and E. T. Won, "100-mb/s nrz visible light communications using a postequalized white led," *IEEE Photonics Technology Letters*, vol. 21, no. 15, pp. 1063–1065, 2009.

[60] S. Watson, M. Tan, S. P. Najda, P. Perlin, M. Leszczynski, G. Targowski, S. Grzanka, and A. E. Kelly, "Visible light communications using a directly modulated 422 nm gan laser diode," *Opt. Lett.*, vol. 38, no. 19, pp. 3792–3794, Oct 2013.

[61] C. Lee, C. Zhang, M. Cantore, R. M. Farrell, S. H. Oh, T. Margalith, J. S. Speck, S. Nakamura, J. E. Bowers, and S. P. DenBaars, "4 gbps direct modulation of 450 nm gan laser for high-speed visible light communication," *Opt. Express*, vol. 23, no. 12, pp. 16 232–16 237, Jun 2015.